Eur. Phys. J. C (2020) 80:195
https://doi.org/10.1140/epjc/s10052-020-7617-3

THE EUROPEAN PHYSICAL JOURNAL C

Special Article - Tools for Experiment and Theory

openQ*D code: a versatile tool for QCD+QED simulations

RC*OR collaboration

Isabel Campos[1], Patrick Fritzsch[2,a], Martin Hansen[3], Marina Krstic Marinkovic[4], Agostino Patella[5], Alberto Ramos[4], Nazario Tantalo[3,6]

[1] Instituto de Física de Cantabria and IFCA-CSIC, Avda. de Los Castros s/n, 39005 Santander, Spain
[2] Theoretical Physics Department, CERN, 1211 Geneva 23, Switzerland
[3] INFN, Sezione di Tor Vergata, Via della Ricerca Scientifica 1, 00133 Rome, Italy
[4] School of Mathematics, Trinity College Dublin, Dublin 2, Ireland
[5] Institut für Physik and IRIS Adlershof, Humboldt Universität zu Berlin, Zum Grossen Windkanal 6, 12489 Berlin, Germany
[6] Dipartimento di Fisica, Università di Roma Tor Vergata, Via della Ricerca Scientifica 1, 00133 Rome, Italy

Received: 12 September 2019 / Accepted: 6 January 2020
© The Author(s) 2020

Abstract We present the open-source package openQ*D-1.0 (openQ*D. GitLab: https://gitlab.com/rcstar/openQxD. CSIC: https://dx.doi.org/10.20350/digitalCSIC/8591. https://hdl.handle.net/10261/173334, 2019), which has been primarily, but not uniquely, designed to perform lattice simulations of QCD+QED and QCD, with and without C* boundary conditions, and $O(a)$ improved Wilson fermions. The use of C* boundary conditions in the spatial direction allows for a local and gauge-invariant formulation of QCD+QED in finite volume, and provides a theoretically clean setup to calculate isospin-breaking and radiative corrections to hadronic observables from first principles. The openQ*D code is based on openQCD-1.6 (Simulation program for lattice QCD (openQCD code). https://cern.ch/luscher/openQCD, 2016) and NSPT-1.4 (Numerical Stochastic Perturbation Theory (NSPT code). https://cern.ch/luscher/NSPT, 2017). In particular it inherits from openQCD-1.6 several core features, e.g. the highly optimized Dirac operator, the locally deflated solver, the frequency splitting for the RHMC, or the 4th order OMF integrator.

Contents

1 Introduction

QED radiative corrections to hadronic observables are generally rather small but they become phenomenologically relevant when the target precision is at the percent level. For example, the leptonic and semileptonic decay rates of light pseudoscalar mesons are measured with a very high accuracy and, on the theoretical side, have been calculated

[a] e-mail: fritzsch@uni-muenster.de (corresponding author)

with the required non-perturbative accuracy by many lattice collaborations. Most of these calculations have been performed by simulations of lattice QCD without taking into account QED radiative corrections. A recent review [4] of the results obtained by the different lattice groups shows that leptonic and semileptonic decay rates of π and K mesons are presently known at the sub-percent level of accuracy. At the same time, QED radiative corrections to these quantities are estimated to be of the order of a few percent, by means of chiral perturbation theory [5]. These estimates have recently been confirmed in the case of the leptonic decay rates of π and K by a first-principle lattice calculation of the QED radiative corrections at $O(\alpha)$ in Refs. [6,7].

Other remarkable examples of observables for which QED radiative corrections are phenomenologically relevant are the so-called lepton flavour universality ratios. For example $R(D^{(*)})$ is defined as the branching ratio for $B \mapsto D^{(*)}\ell\bar{\nu}_\ell$ with $\ell = e, \mu$ divided by the branching ratio for $B \mapsto D^{(*)}\tau\bar{\nu}_\tau$. Most of the hadronic uncertainties cancel in these ratios that are built in such a way that they are trivial in the Standard Model, in the limit in which the two leptons have the same mass. Presently, a combined analysis [8] of the $R(D)$ and $R(D^*)$ ratios shows a deviation of the experimental measurements from the theoretical predictions of the order of 3 standard deviations. On the other hand, QED radiative corrections are different for the two leptons because of the different masses and an improved theoretical treatment of these effects (see for example Refs. [9,10] for a discussion of this point) can possibly enhance or reconcile the observed discrepancy between the experimental measurements and the theoretical expectations.

QED radiative corrections to hadronic observables can be computed from first principles by performing lattice simulations of QCD coupled to QED, treating the photon field on an equal footing as the gluon field. Since these corrections are expected to be at the percent level, in order to resolve them against the statistical noise, one needs to simulate at various values of the fine-structure constant and to interpolate to the physical value. This approach, pioneered in Refs. [11–13], is highly non-trivial from both the numerical and theoretical point of view, because of the peculiarities of QED. Numerically, lattice calculations are unavoidably affected by statistical and systematic uncertainties and it can be challenging to resolve QED radiative corrections from the leading QCD contributions within the errors of a simulation. Theoretically, a big issue arises because lattice calculations have necessarily to be done on a finite volume. QED is a long-range interaction and, consequently, finite-volume effects are the key issue in presence of electromagnetic interactions.

In fact, as a consequence of Gauss' law, it is impossible to have a net electric charge on a periodic torus. Because of this strong theoretical constraint, it is particularly challenging to calculate from first principles physical observables associated with electrically charged external states, such as the phenomenologically relevant quantities discussed above. Several approaches have been proposed over the years to cope with this problem, see Ref. [14] for a recent review. The most popular approaches to the problem of charged particles on the torus solve the Gauss' law constraint by introducing non-local terms in the finite-volume action of the theory.[1] The effects induced by the non-locality of the action are expected to disappear once the infinite-volume limit is properly taken and, as far as $O(\alpha)$ QED radiative corrections are concerned, it is generally possible to show that this is indeed the case.

On the one hand, the non-local formulations of the theory are particularly appealing because of their formal simplicity. On the other hand, it has been shown in Ref. [18] that it is possible to probe electrically charged states on a finite volume by starting from a local formulation of the theory and, remarkably, in a fully gauge-invariant way. This is possible by using C-parity (or C*) boundary conditions for all the fields and by using a certain class of interpolating operators originally introduced by Dirac in a seminal work [19] on the canonical quantization of QED.

The formulation of Ref. [18] has also been studied numerically. The results for the meson masses extracted in a fully gauge-invariant way from lattice simulations of QCD+QED with C* boundary conditions obtained in Ref. [20] provide a convincing numerical evidence that, beside being an attractive theoretical formulation, the proposal of Ref. [18] is also a valid numerical alternative for the calculation of QED radiative corrections on the lattice. This motivated the present work.

In this paper we present the open-source package `openQ*D`, which can be used to simulate QCD+QED, QCD, the pure SU(3) and U(1) gauge theories.[2] The code allows to choose a wide variety of temporal and spatial boundary conditions. In particular, it allows to perform dynamical simulations of QCD+QED with C* but also with periodic boundary conditions along the spatial directions. Simulations of QCD with C* boundary conditions can be a valuable starting point for the application of the RM123 method [21], in which observables are calculated order-by-order in the electromagnetic coupling. A fully tested and stable release of `openQ*D` can be downloaded from [1].

The `openQ*D` package is based on the `openQCD`[2] package from which it inherits the core features, most notably the implementation of the Dirac operator, of the solvers and the possibility of simulating open and Schrödinger func-

[1] A different approach is based on the idea that one can write QCD+QED observables at first order in α as QCD observables with analytic (possibly infinite-volume) QED kernels, e.g. [15–17].

[2] The code allows also for (inefficient) simulations of QED in isolation, even though a main program for this purpose is not provided in the 1.0 version.

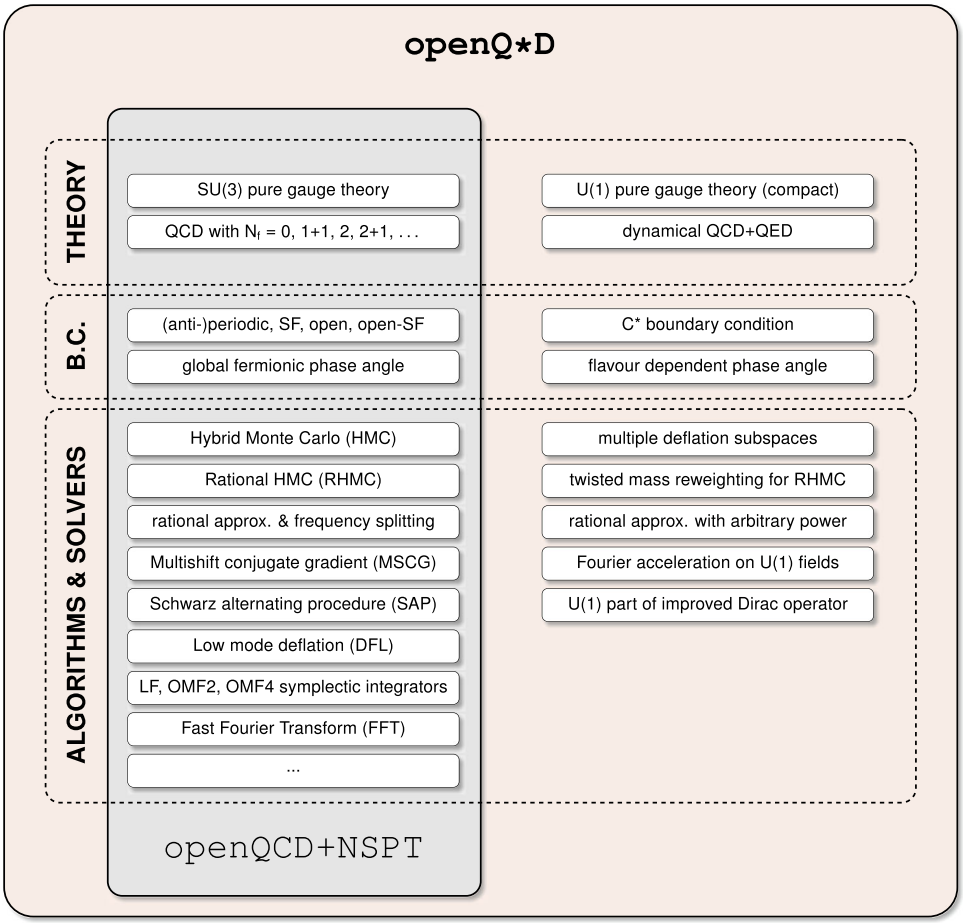

Fig. 1 Summary of salient features of `openQ*D`. Some features inherited from `openQCD` and `NSPT` are highlighted

tional boundary conditions in the time direction. One of the inherited solvers implements the inexact deflation algorithm of Ref. [22]. An added value of the `openQ*D` package is the possibility of using more deflation subspaces in a single simulation. This is particularly important in the case of QCD+QED simulations because different deflation subspaces have to be generated for quarks having different electric charges.

Another important feature present in the `openQ*D` package is the possibility to use Fourier Acceleration [23,24] for the molecular dynamics evolution of the U(1) field. The used implementation of the Fast Fourier Transform (FFT) is an adaptation of the corresponding module in the `NSPT` [3,25] package.

The remaining of this paper is organised as follows. In Sect. 2 we give an overview of the theoretical background needed to understand the actions simulated by `openQ*D`, and we describe some peculiar aspects of the simulation algorithm. In particular, the specific implementation of C* boundary conditions and of the Fourier Acceleration for the U(1) field are discussed. In Sect. 3 we provide instructions on how to compile the code, construct a sample input file, and run the program that generates QCD+QED configurations. Section 4 is a collection of tests and performance studies. In particular, we present scalability tests, and studies of the performance of solvers for the Dirac equation for electrically charged fields. We also illustrate the outcome of some sample runs performed for testing purposes. In Fig. 1, we provide a schematic view of the `openQ*D` functionalities.

2 Theoretical background

An overview of the main algorithmic choices made in the code will be given in this section. The fundamental fields are the SU(3) link variable $U_\mu(x)$ and the real photon field $A_\mu(x)$. Since only the compact formulation of QED is implemented at present, all observables are written in terms of the U(1) link variable

$$z_\mu(x) = \exp\{i A_\mu(x)\}, \tag{2.1}$$

which implies that the real photon field can be restricted to $-\pi \le A_\mu(x) \le \pi$ with no loss of generality. Various boundary conditions can be chosen for the gauge fields: periodic, open [26], Schrödinger Functional (SF) [27,28] and open-

SF boundary conditions [29] in the Euclidean time direction $\mu = 0$, periodic and C* boundary conditions [30–33] in the spatial directions. The implementation of C* boundary conditions is discussed in Sect. 2.1.

After integrating out the fermion fields in a usual way, the target distribution of QCD+QED if no C* boundary conditions are used is

$$\rho_{\rm tar}(U, A) \propto e^{-S_{\rm g,SU(3)}(U)-S_{\rm g,U(1)}(A)} \prod_f \det D_f, \tag{2.2}$$

where the gauge actions $S_{\rm g,SU(3)}(U)$ and $S_{\rm g,U(1)}(A)$ are briefly discussed in Sect. 2.2, the product runs over the simulated fermion flavours indicized by f, and the Dirac operator D is introduced in Sect. 2.3. If C* boundary conditions are used, the determinant is replaced by a Pfaffian, i.e.

$$\rho_{\rm tar}(U, A) \propto e^{-S_{\rm g,SU(3)}(U)-S_{\rm g,U(1)}(A)} \prod_f {\rm pf}\,(CTD_f), \tag{2.3}$$

where C is the charge conjugation matrix and T is a field-independent matrix satisfying $T^2 = 1$, whose detailed definition can be found in Sect. 2.1. While in the continuum limit the determinant and the Pfaffian are positive, this is not the case with Wilson fermions. The absolute value is considered in both cases, which amounts to replacing

$$\begin{aligned} &\det D_f \to \left|\det D_f\right|, \\ &{\rm pf}\,(CTD_f) \to \left|{\rm pf}\,(CTD_f)\right| = \left|\det D_f\right|^{1/2}. \end{aligned} \tag{2.4}$$

The sign should be separately calculated and included in the evaluation of observables as a reweighting factor [34,35]. It is important to stress that this is a mild sign problem [18], which becomes irrelevant sufficiently close to the continuum limit, and which is also present in standard QCD simulations for the strange quark. The presented strategy is in line with state-of-the-art QCD and QCD+QED simulations, in which the sign of the determinant is simply ignored. Future work will be planned to investigate the importance of the sign especially at lighter quark masses.

After introducing the standard even–odd preconditioned operator $\hat{D}$ [36], one rewrites the quark part of the distribution as

$$\begin{aligned} \prod_f \left|\det D_f\right|^{2\alpha_f} &= \prod_f \det(D_f^\dagger D_f)^{\alpha_f} \\ &= e^{-S_{\rm sdet}(U,A)} \prod_f \det(\hat{D}_f^\dagger \hat{D}_f)^{\alpha_f}, \end{aligned} \tag{2.5}$$

where α_f is either $1/2$ or $1/4$. The definitions of $\hat{D}_f$ and $S_{\rm sdet}$ can be found in Sect. 2.3. Instead of this target distribution, the `openQ*D` code simulates a slightly different distribution

$$\rho_{\rm sim}(U, A) \propto e^{-S_{\rm g,SU(3)}(U)-S_{\rm g,U(1)}(A)} e^{-S_{\rm sdet}(U,A)} \prod_f \det R_f^{-1}. \tag{2.6}$$

written in terms of a rational approximation R_f [37]

$$R_f \simeq (\hat{D}_f^\dagger \hat{D}_f + \mu_f^2)^{-\alpha_f}, \tag{2.7}$$

where μ_f is a tunable parameter introduced to suppress configurations with exceptionally small eigenvalues of $\hat{D}_f^\dagger \hat{D}_f$ (*twisted-mass reweighting* [26,38]). If μ_f is small enough and the rational approximation is accurate enough, the simulated distribution $\rho_{\rm sim}(U, A)$ is very close to the target one $\rho_{\rm tar}(U, A)$. The difference is corrected by means of reweighting factors W_f

$$\frac{\rho_{\rm tar}(U, A)}{\rho_{\rm sim}(U, A)} \propto \prod_f W_f, \qquad W_f = \det\left[(\hat{D}_f^\dagger \hat{D}_f)^{\alpha_f} R_f\right], \tag{2.8}$$

which have to be separately calculated and included in the expectation values of observables as follows

$$\langle O \rangle_{\rm tar} = \frac{\langle O \prod_f W_f \rangle}{\langle \prod_f W_f \rangle}. \tag{2.9}$$

The detailed discussion of the supported reweighting factors can be found in Appendix A. The rational function R_f can be decomposed in a product of positive factors $R_{f,\ell}$ (*frequency splitting* [26]). More details on frequency splitting are provided in Sect. A.2. The determinant of the rational functions is finally represented by means of a pseudofermion quadratic action as in

$$\det R_f^{-1} = \prod_\ell \det R_{f,\ell}^{-1} = \int [d\Phi]\, e^{-\sum_\ell (\Phi_{f,\ell}, R_{f,\ell}\Phi_{f,\ell})}. \tag{2.10}$$

The distribution is generated by means of a Hybrid Monte Carlo (HMC) algorithm with Fourier acceleration for the U(1) field. The molecular dynamics (MD) Hamiltonian is given by

$$H = \frac{1}{2}(\pi, \Delta^{-1}\pi)_{\rm U(1)} + \frac{1}{2}(\Pi, \Pi)_{\rm SU(3)} + S(U, A, \Phi), \tag{2.11}$$

where $\Pi_\mu(x)$ and $\pi_\mu(x)$ denote the momentum fields associated to the SU(3) and U(1) fields, the operator $(-\Delta)$ is a discretization of the Laplace operator, and the action is given by

$$\begin{aligned} S(U, A, \Phi) = {} & S_{\rm g,SU(3)}(U) + S_{\rm g,U(1)}(A) + S_{\rm sdet}(U, A) \\ & + \sum_{f,\ell} (\Phi_{f,\ell}, R_{f,\ell}\Phi_{f,\ell}). \end{aligned} \tag{2.12}$$

Details on the implementation of the Fourier acceleration are presented in Appendix B. The HMC consists of three steps.

1. The momentum and pseudofermion fields are randomly generated with probability distribution given by e^{-H};
2. The gauge fields are evolved with a discretized version of the MD equations, i.e.

$$\begin{aligned}\partial_t A_\mu(x) &= \Delta^{-1}\pi_\mu(x)\\ \partial_t U_\mu(x) &= \Pi_\mu(x)U_\mu(x)\\ \partial_t \pi_\mu(x) &= -\partial_{A_\mu(x)}S(U,A,\Phi),\\ \partial_t \Pi_\mu(x) &= -\partial_{U_\mu(x)}S(U,A,\Phi),\end{aligned} \tag{2.13}$$

where $\partial_{U_\mu(x)}$ is the left Lie derivative with respect to $U_\mu(x)$ while $\partial_{A_\mu(x)}$ is the elementary derivative with respect to $A_\mu(x)$. In practice multiple time-scale [39] symplectic integrators are used to solve the MD equation: leapfrog, 2nd and 4th order Omelyan–Mryglod–Folk integrators [40] are available (LF, OMF2, OMF4).
3. The evolved gauge configuration is accepted or rejected with a standard Metropolis test with probability distribution given by e^{-H}.

2.1 C* boundary conditions

Other than the variety of boundary conditions in the temporal direction inherited from `openQCD-1.6`, the `openQ*D` code allows for periodic or C* boundary conditions to be chosen in the spatial directions. If the gauge fields satisfy periodic boundary conditions in *all* spatial directions k, the fermion fields $\psi_f(x)$ and $\bar\psi_f(x)$ satisfy general phase-periodic boundary conditions (f is the flavour index), i.e.

$$\begin{aligned}U_\mu(x+L_k\hat e_k) &= U_\mu(x),\\ A_\mu(x+L_k\hat e_k) &= A_\mu(x),\\ \psi_f(x+L_k\hat e_k) &= e^{i\theta_{f,k}}\psi_f(x),\\ \bar\psi_f(x+L_k\hat e_k) &= e^{-i\theta_{f,k}}\bar\psi_f(x).\end{aligned} \tag{2.14}$$

Phase-periodic boundary conditions are incompatible with C* boundary conditions. If the gauge fields satisfy C* boundary conditions in at least one direction, say k, then $\theta_{f,j}=0$ for all f and j, and

$$\begin{aligned}U_\mu(x+L_k\hat e_k) &= U^*_\mu(x),\\ A_\mu(x+L_k\hat e_k) &= -A_\mu(x),\\ \psi_f(x+L_k\hat e_k) &= C^{-1}\bar\psi^T_f(x),\\ \bar\psi_f(x+L_k\hat e_k) &= -\psi^T_f(x)C.\end{aligned} \tag{2.16}$$

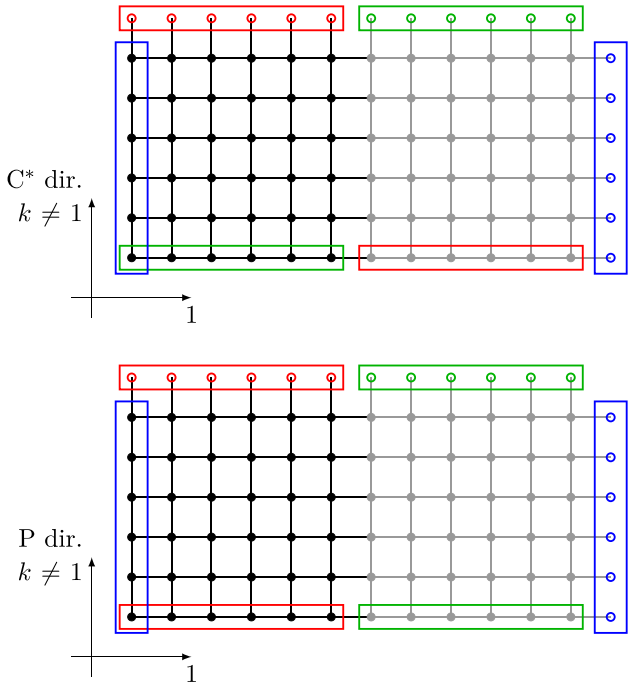

Fig. 2 Global geometry of extended lattice. The *top diagram* represents a section of the extended lattice along a $(1,k)$ plane where $k=2,3$ is a direction with C* boundary conditions. All fields are periodic along the extended direction 1. C* boundary conditions in the direction $k=2,3$ are replaced by shifted boundary conditions in the extended lattice. Shifted boundary conditions are imposed by properly defining the nearest neighbours of boundary sites. Empty circles in the red (resp. green, blue) rectangle have to be identified with the corresponding solid circles in the red (resp. green, blue) rectangle. The *bottom diagram* represents a section of the extended lattice along a $(1,k)$ plane where $k=2,3$ is a periodic direction. In *both diagrams*, the black circles represent the sites of the physical lattice, and the grey circles represent the sites of the mirror lattice

The charge-conjugation matrix C satisfies

$$C^T=-C,\qquad C^\dagger=C^{-1},\qquad C^{-1}\gamma_\mu C=-\gamma_\mu^T. \tag{2.18}$$

C* boundary conditions are implemented by means of an orbifold construction. Assume that $k=1$ is a direction with C* boundary conditions,[3] in order to simulate a *physical lattice* with size $V=L_0\times L_1\times L_2\times L_3$ the `openQ*D` code allocates a lattice with size $V_{C^*}=L_0\times(2L_1)\times L_2\times L_3$, which we will refer to as the *extended lattice*. Points in the *physical lattice* are assumed to have coordinates which satisfy $0\le x_\mu<L_\mu$. The extended lattice can be interpreted as a double-covering of the physical lattice, with coordinates satisfying $0\le x_\mu<L_\mu$ for $\mu\neq 1$ and $0\le x_1<2L_1$. Points outside the physical lattice constitute the *mirror lattice*. On

[3] In the input file of a typical main program in `openQ*D` (see Sect. 3.2), one can choose the number of spatial directions with C* boundary conditions. C* boundary conditions are turned on sequentially in directions 1, 2 and 3.

the extended lattice, points x and $x + L_k\hat{e}_k$ do not coincide, so Eqs. (2.16) and (2.17) have to be interpreted as constraints which define the admissible gauge and fermion fields. These are referred to as the *orbifold constraints*. While the admissible gauge fields in the mirror lattice are completely determined by the value of the gauge field in the physical lattice via (2.16), the orbifold constraint has a different meaning for fermion fields, providing a relation between ψ in the physical lattice and $\bar{\psi}$ in the mirror lattice, and vice versa. Given that the fermion fields ψ and $\bar{\psi}$ are independent Grassmanian variables on the physical lattice, then one can equivalently choose the value of ψ in each point of the extended lattice as a complete set of independent variables. The integration of the Grassmanian variables yields the Pfaffian of the operator CTD [18], where T is the translation operator defined by

$$T\psi(x) = \psi(x + L_1\hat{e}_1). \tag{2.19}$$

One easily proves that

$$|\mathrm{pf}\,(CTD)| = |\det D|^{1/2}\,, \tag{2.20}$$

which justifies the need for $\alpha_f = 1/4$ in Eq. (2.5). Since the square of the charge-conjugation operation is the identity, all fields must obey periodic boundary conditions along the extended direction $k = 1$, i.e.

$$U_\mu(x + 2L_1\hat{e}_1) = U_\mu(x), \qquad A_\mu(x + 2L_1\hat{e}_1) = A_\mu(x), \tag{2.21}$$

$$\psi_f(x + 2L_1\hat{e}_1) = \psi_f(x), \qquad \bar{\psi}_f(x + 2L_1\hat{e}_1) = \bar{\psi}_f(x). \tag{2.22}$$

C* boundary conditions in directions $k = 2, 3$ are implemented by modifying the global topology of the extended lattice (see Fig. 2). In fact in these directions, C* boundary conditions in the physical lattice imply shifted boundary conditions in the extended lattice, i.e.

$$\begin{aligned} U_\mu(x + L_k\hat{e}_k) &= U_\mu(x + L_1\hat{e}_1), \\ A_\mu(x + L_k\hat{e}_k) &= A_\mu(x + L_1\hat{e}_1), \end{aligned} \tag{2.23}$$

$$\begin{aligned} \psi_f(x + L_k\hat{e}_k) &= \psi_f(x + L_1\hat{e}_1), \\ \bar{\psi}_f(x + L_k\hat{e}_k) &= \bar{\psi}_f(x + L_1\hat{e}_1). \end{aligned} \tag{2.24}$$

When the determinant of the Dirac operator is stochastically estimated by means of a pseudofermion action as in Eq. (2.12), the pseudofermion field $\Phi_{f,\ell}$ is natively defined on the extended lattice, i.e. $\Phi_{f,\ell}(x)$ are truly independent variables for each x in the extended lattice. Moreover it satisfies the same boundary conditions as ψ_f in Eqs. (2.22) and (2.24).

It is worth noticing that C* boundary conditions can be implemented in different ways. For instance, the implementation proposed in Appendix D of Ref. [18] does not double the lattice, but the number of pseudofermion fields. Roughly speaking one needs to represent quarks and antiquarks by means of independent pseudofermion fields which are mixed by the boundary conditions. The `openQ*D` implementation simply maps each pair of pseudofermion fields in the geometry of the extended lattice. The cost of the application of the Dirac operator implemented as in `openQ*D` and as in [18] is exactly identical. Therefore, as far as the application and inversion of the Dirac operator, the orbifold construction does not introduce any overhead with respect to more standard implementations of C* boundary conditions. On the other hand, the gauge field is evolved twice. In principle one could evolve the gauge field only on the physical lattice and then copy its value to the mirror lattice. This strategy will be considered in the future. However, simulations close to the physical point are dominated by the inversion of the Dirac operator and the overhead due to the evolution of the gauge field is expected to be negligible. Evidence of this fact has been presented in [41]. The orbifold construction has been chosen essentially because it requires only minimal modifications of the `openQCD` code. In fact the functions that impose the orbifold constraint on gauge and momentum fields are trivial, shifted boundary conditions (by half lattice) are implemented by a simple redefinition of the map of nearest neighbouring MPI processes, and finally gauge action and forces need to be multiplied by a factor 1/2. On the other hand the Dirac operators and the solvers are completely untouched by the orbifold construction.

2.2 Gauge actions

The SU(3) and compact U(1) gauge actions that can be simulated with `openQ*D` are

$$S_{\mathrm{g,SU(3)}} = \frac{\omega_{\mathrm{C}^*}}{g_0^2}\sum_{k=0}^{1} c_k^{\mathrm{SU(3)}} \sum_{\mathcal{C}\in\mathcal{S}_k} \mathrm{tr}\,[1 - U(\mathcal{C})], \tag{2.25}$$

$$S_{\mathrm{g,U(1)}} = \frac{\omega_{\mathrm{C}^*}}{2q_{\mathrm{el}}^2 e_0^2}\sum_{k=0}^{1} c_k^{\mathrm{U(1)}} \sum_{\mathcal{C}\in\mathcal{S}_k} [1 - z(\mathcal{C})], \tag{2.26}$$

where $U(\mathcal{C})$ and $z(\mathcal{C})$ denote the SU(3) and U(1) parallel transports along a path $\mathcal{C}$ on the lattice. $\mathcal{S}_0$ and $\mathcal{S}_1$ are the sets of all oriented plaquettes and all oriented 1×2 planar loops respectively and the overall weight ω_{C^*} is 1 if no C* boundary conditions are used. With C* boundary conditions $\omega_{\mathrm{C}^*} = 1/2$ corrects for the double counting introduced by summing over all plaquette and double-plaquette loops in the extended lattice instead of the physical lattice (c.f. Sect. 2.1). The coefficients $c_{0,1}$ satisfy the relation $c_0 + 8c_1 = 1$. For SU(3), the Wilson action is obtained by choosing $c_0 = 1$, the tree-level improved Symanzik (or Lüscher–Weisz) action is obtained by choosing $c_0 = \frac{5}{3}$, and the Iwasaki action is obtained by choosing $c_0 = 3.648$. The parameters g_0 and e_0 are the bare SU(3) and U(1) gauge couplings respec-

tively, which are related to the β parameter and the bare fine-structure constant α_0 by

$$\beta = \frac{6}{g_0^2}, \quad \alpha_0 = \frac{e_0^2}{4\pi}. \tag{2.27}$$

In the compact formulation of QED, all electric charges must be integer multiples of some elementary charge $q_{\rm el}$ which is defined in units of the charge of the positron. As discussed in Ref. [18], $q_{\rm el}$ appears as an overall factor in the gauge action and essentially sets the normalization of the U(1) gauge field in the continuum limit. Even though in infinite volume $q_{\rm el} = 1/3$ would be an appropriate choice in order to simulate quarks, in finite volume with C* boundary conditions one needs to choose $q_{\rm el} = 1/6$ in order to construct gauge-invariant interpolating operators for charged hadrons [18,20]. Note that by using a compact formulation of QED, no gauge fixing is added to the action, and furthermore the user is free to choose simulating (QCD+)QED without C* boundary conditions.

The actions in Eqs. (2.25) and (2.26) assume periodic boundary conditions in time. In the more general case, the actions are modified at the time boundary in order to allow for $O(a)$ improvement. The general form of the gauge actions can be found in [42].

2.3 Dirac operator

The Dirac operator implemented in `openQ*D` is given by a sum of terms

$$D = m_0 + D_{\rm w} + \delta D_{\rm sw} + \delta D_{\rm b}, \tag{2.28}$$

where $D_{\rm w}$ is the (unimproved) Wilson–Dirac operator, $\delta D_{\rm sw}$ is the Sheikholeslami–Wohlert (SW) term, and $\delta D_{\rm b}$ is the time boundary $O(a)$-improvement term. For simplicity, periodic boundary conditions in the time direction will be assumed, which means $\delta D_{\rm b} = 0$. The definition of $\delta D_{\rm b}$ for other boundary conditions can be found in [43]. The Wilson–Dirac operator of Eq. (2.28) can be written as

$$D_{\rm w} = \sum_{\mu=0}^{3} \frac{1}{2} \left\{ \gamma_\mu (\nabla_\mu + \nabla_\mu^*) - \nabla_\mu^* \nabla_\mu \right\}, \tag{2.29}$$

where the covariant derivatives are defined as

$$\nabla_\mu \psi(x) = U(x,\mu) z(x,\mu)^{\hat{q}} \psi(x+\hat{\mu}) - \psi(x), \tag{2.30}$$

$$\nabla_\mu^* \psi(x) = \psi(x) - U(x-\hat{\mu},\mu)^\dagger z(x-\hat{\mu},\mu)^{-\hat{q}} \psi(x-\hat{\mu}). \tag{2.31}$$

The SW term is given by

$$\delta D_{\rm sw} = c_{\rm sw}^{\rm SU(3)} \sum_{\mu,\nu=0}^{3} \tfrac{i}{4} \sigma_{\mu\nu} \hat{F}_{\mu\nu} + q\, c_{\rm sw}^{\rm U(1)} \sum_{\mu,\nu=0}^{3} \tfrac{i}{4} \sigma_{\mu\nu} \hat{A}_{\mu\nu}. \tag{2.32}$$

The SU(3) field tensor $\hat{F}_{\mu\nu}(x)$ and the U(1) field tensor $\hat{A}_{\mu\nu}(x)$ are constructed in terms of the clover plaquette. The explicit expression of the SU(3) field tensor used in `openQ*D` can be found in Ref. [44], while the U(1) field tensor is given here,

$$\hat{A}_{\mu\nu}(x) = \tfrac{i}{4q_{\rm el}} {\rm Im} \left\{ z_{\mu\nu}(x) + z_{\mu\nu}(x-\hat{\mu}) + z_{\mu\nu}(x-\hat{\nu}) + z_{\mu\nu}(x-\hat{\mu}-\hat{\nu}) \right\}, \tag{2.33}$$

$$z_{\mu\nu}(x) = z(x,\mu) z(x+\hat{\mu},\nu) z(x+\hat{\nu},\mu)^\dagger z(x,\nu)^\dagger. \tag{2.34}$$

The normalization is chosen in such a way that $-ie_0 \hat{A}_{\mu\nu}(x)$ is the canonically-normalized field tensor in the naive continuum limit. Notice that the field tensors are anti-hermitian.

In presence of electromagnetism, the Dirac operator depends on the electric charge of the quark field. Let q be the physical electric charge in units of e (i.e. $q = 2/3$ for the up quark, and $q = -1/3$ for the down quark). In the compact formulation of QED, all electric charges must be integer multiples of an elementary charge $q_{\rm el}$, which appears as a parameter in the U(1) gauge action (2.26). The integer parameter

$$\hat{q} = \frac{q}{q_{\rm el}} \in \mathbb{Z} \tag{2.35}$$

is the one appearing in the hopping term in Eqs. (2.30) and (2.31). On the other hand, notice that the SW term (2.32) is written in terms of the physical charge q. This normalization corresponds to a definition of $c_{\rm sw}^{\rm U(1)}$ which is equal to 1 at tree level. The definition of the even–odd preconditioned Dirac operator $\hat{D}$ is standard [36]

$$\hat{D} = D_{\rm ee} - D_{\rm eo} D_{\rm oo}^{-1} D_{\rm oe}, \qquad D = \begin{pmatrix} D_{\rm ee} & D_{\rm eo} \\ D_{\rm oe} & D_{\rm oo} \end{pmatrix} \tag{2.36}$$

and so is the definition of the *small-determinant* action $S_{\rm sdet}$ appearing in Eq. (2.5)

$$S_{\rm sdet} = -\sum_f \alpha_f \, {\rm tr} \, \log(\mathbf{1} + D_{f,{\rm oo}}). \tag{2.37}$$

3 Simulating QCD+QED with `openQ*D`

3.1 Structure of the `openQ*D` program package

The `openQ*D` code includes several main programs, roughly divided in three categories: programs to generate configurations, programs to measure observables, and utility programs. The following programs (in the `main` directory) can be used to generate gauge configurations for various theories:

- `iso1`: SU(3)×U(1) gauge theory with dynamical fermions;
- `qcd1`: SU(3) gauge theory with dynamical fermions;

- `ym1`: SU(3) pure gauge theory;
- `mxw1`: U(1) pure gauge theory.

The following programs (in the `main` directory) can be used to calculate simple observables:

- `ms1`: reweighting factors (see Sect. 3.2 and Appendix A);
- `ms2`: spectral range of $(\hat{D}^\dagger \hat{D})^{1/2}$ ($\hat{D}$ is the even–odd preconditioned Dirac operator);
- `ms3`: SU(3) Wilson-flow observables;
- `ms4`: quark propagators;
- `ms5`: U(1) Wilson-flow observables;
- `ms6`: neutral pseudoscalar–pseudoscalar and axial–pseudoscalar correlators.

Finally, the following utility programs are also included:

- `minmax/minmax`: it generates the rational approximations needed for the RHMC algorithm;
- `devel/nompi/read*`: they can be used to read the binary `*.dat` files generated by the other programs.

3.2 User guide for the dynamical QCD+QED simulation program `iso1`

3.2.1 Compiling and running the main program

A complete guide to the usage of all programs listed in Sect. 3.1 can be found in the headers of the source-code files, and in the `README` files in the corresponding directories. Often the user will be referred to other sources of documentation (e.g. `README` files in some of the `modules` subdirectories, or the headers of other source-code files, and some of the PDF files in the `doc` directory). This section is intended to be neither a replacement nor a duplicate of these sources of documentation, but rather an overview of the main steps that are needed to use the `iso1` program to generate QCD+QED configurations.

1. **Download the code and check the dependences.** The code is publicly available on GitLab at https://gitlab.com/rcstar/openQxD. The simulation and measurement programs, i.e. all programs in the `main` directory, require some MPI libraries compliant with the MPI 1.2 (or later) standard. The `minmax` program requires the GMP (https://gmplib.org) and GNU MPFR (http://www.mpfr.org) libraries. Notice that the `minmax` program can be run on a personal computer and does not need MPI, therefore one does not need to install the GMP and GNU MPFR libraries on production machines.
2. **Set the environment variables.** The Makefile in the `main` directory assumes that the C compiler can be called by using `$(GCC)`, the MPI header file is found at `$(MPI_INCLUDE)/mpi.h`, the MPI compiled library is found in the `$(MPI_HOME)/lib/` directory, and the `mpicc` command is available. The needed environment variables can be defined in the appropriate shell initialization files, e.g.

```
#!/bin/bash
# [Stuff]

export GCC="gcc"
export MPI_INCLUDE="/usr/local/
       include/"
export MPI_HOME="/usr/local/"
```

3. **Choose the intrinsics acceleration options.** Some pieces of code exist in several versions: plain C, inline-assembly with SSE instructions, and inline-assembly with AVX instructions. The default Makefile uses the C version of the code. In order to use the inline-assembly version, one needs to modify the `CFLAGS` variable defined in lines 122–124 of `main/Makefile`. For instance, on some x86-64 machines one can use

```
122 CFLAGS = -std=c89 -pedantic\
123          -fstrict-aliasing \
124          -Wall -Wno-long-long\
125          -Wstrict-prototypes \
126          -Werror -O -mno-avx -DAVX\
127          -DFMA3 -DPM
```

which activates AVX and FMA3 instructions and assumes that prefetch instructions fetch 64 bytes at a time. For a full description of available options, refer to the `README` file in the root directory.

4. **Choose the lattice geometry.** The lattice geometry is chosen at compile time by modifying the macros defined in the first part of the `include/global.h` file. A full description of these macros can be found in the `main/README.global` file. For instance the following choice

```
18 #define NPROC0 8
19 #define NPROC1 8
20 #define NPROC2 4
21 #define NPROC3 4
22
23 #define L0 8
24 #define L1 8
25 #define L2 8
26 #define L3 8
```

corresponds to an 8^4 local lattice, replicated on an $8^2 \times 4^2$ MPI process grid (the code will need to be run with 1024 MPI processes), which yields a $64^2 \times 32^2$ global lattice. As explained in Sect. 2.1, this choice of simulation parameters corresponds to a $64^2 \times 32^2$ physical global lattice if no C* boundary conditions are used, or to a 64×32^3 physical global lattice if C* boundary conditions are used in at least one spatial direction. In our

implementation, NPROCn has to be a multiple of 2 if C* boundary conditions are used in the direction n = 1, 2, 3.

5. **Compile the `iso1` program and prepare for running.** At this point, the code is ready to be compiled. Assuming that the root directory of the code is $HOME/openQxD, this is done by executing the following commands in a bash shell.

```
cd ${HOME}/openQxD/main
make iso1
```

One can set up the directories and files to run the code by executing the following commands in a bash shell.

```
cd ${HOME}/openQxD
mkdir test
cd test
mkdir cnfg dat log input
cp ../main/iso1 iso1
> input/pedro01.in
> runtest.sh
chmod a+x runtest.sh
```

6. **Edit the input file.** The input file input/pedro01.in must contain all adjustable parameters of the simulation (except the few ones that have been set at compile time). A rough guide on how to construct an input file for the iso1 program is found in Sect. 3.2.2. Alternatively, a sample input file can be cut and paste from Appendix C.
7. **Start the simulation.** Edit the runtest.sh script as follows:

```
#!/bin/bash
./iso1 -i input/pedro01.in -noloc
   -rmold
```

The runtest.sh script contains the command that invokes the iso1 program. It can be launched via a standard mpirun command, or incorporated in a script for a job scheduler. Recall that the number of needed MPI processes has been decided at compile time, and it is equal to 1024 in this case. The iso1 program takes a number of command-line options: the input file is specified with the -i option, the -noloc option specifies that the configuration files must be saved by a single MPI process, the -rmold specifies that only the most recent configuration must be kept and all previous ones must be deleted. The program will start the simulation from a randomly generated configuration. More details about the command-line options can be found in the main/README.iso1 file.

8. **Interrupt the simulation.** Assuming that no error is produced, the simulation code will end naturally when all the configurations requested in the input file are generated. If the simulation needs to be interrupted earlier, one can just execute the following commands in a bash shell.

```
cd ${HOME}/openQxD/test
touch log/pedro01.end
```

The simulation code will stop gracefully right after the next configuration is saved.

9. **Resume the simulation.** Assuming that the last generated configuration was pedro01n42, edit the input file and set the nth variable in the [MD trajectories] section to 0 (see below for a description of the input file), and edit the runtest.sh script as follows:

```
#!/bin/bash
./iso1 -i input/pedro01.in -noloc
   -rmold -c pedro01n42 -a
```

Once this is executed, the simulation will continue from where it was interrupted.

3.2.2 *Constructing the input file for iso1*

Most of the parameters needed to generate configurations are passed to the iso1 program by means of a human-readable input file, in this case pedro01.in in the test/input directory. For a full description of the various parameters, the reader is referred to the main/README.iso1 and doc/parms.pdf files (and references therein). A rough guide to the various sections that compose the input file is provided here, with no ambition of completeness.

1. **Run name and output directories.**

```
[Run name]
name        pedro01

[Directories]
log_dir     ./log   # absolute path, or relative path
dat_dir     ./dat   # to the working directory of iso1
cnfg_dir    ./cnfg
```

The program iso1 will produce several output files:

- ./log/pedro01.log, human-readable file, with general information about the simulation;
- ./dat/pedro01.dat, binary file, with the history of simple diagnostic observables;
- ./dat/pedro01.ms3.dat and ./dat/pedro01.ms5.dat, binary files, with the history of SU(3) and U(1) Wilson flow observables;
- ./dat/pedro01.par, binary file, with all simulation parameters;
- ./dat/pedro01.rng, binary file, with the state of the random number generator at the time of the most recent saved configuration;
- ./cnfg/pedro01n*, binary files, with the gauge configuration.

For every file in the log and dat directories, a backup file identified by a tilde at the end of its name is created and updated every time a configuration is saved.

2. **Schedule management.**

```
[M D trajectories]
nth          100        # multiple of dtr_cnfg
ntr          800        # multiple of dtr_cnfg
dtr_log      5
dtr_ms       10         # multiple of dtr_log
dtr_cnfg     50         # multiple of dtr_ms
```

The program `iso1` will print one entry in the log file every 5 MD trajectories, will measure and print Wilson flow observables every 10 MD trajectories, will save a configuration every 50 MD trajectories. The first 100 trajectories are considered of thermalization (no observables are measured), a total of 800 MD trajectories will be generated and 15 configurations will be saved.

3. **Ranlux [45] initialization.**

```
[Random number generator]
level     0         # this should not be changed
seed      19521     # this can be any positive
      integer
```

4. **Boundary conditions.**

```
[Boundary conditions]
type        periodic    # or SF, open, open-SF
cstar       3           # or 0, 1, 2
```

In this case periodic boundary conditions are chosen in time, and C* boundary conditions in all 3 spatial directions. The implementation of C* boundary conditions in `openQ*D` is described in Sect. 2.1. If SF or open-SF boundary conditions are chosen in time, the number of parameters in this section increases, as one needs to specify the value of the fields on the SF boundaries. For a full description of these parameters, refer to `doc/parms.pdf`.

5. **Gauge actions.**

```
[SU(3) action]
beta    5.3
c0      1.0      # 1 = Wilson, 5/3 = Lüscher-Weisz, 3.648 = Iwasaki

[U(1) action]
type    compact  # only option currently available
alpha   0.05     # bare fine-structure constant
invqel  6.0      # see "Quark flavours" below
c0      1.0      # Wilson action
```

If different boundary conditions in time are chosen, the number of parameters in these sections increases, as one needs to specify the $O(a)$-improvement boundary coefficients. Refer to `doc/gauge_action.pdf`, `doc/parms.pdf` of all these parameters.

6. **Quark flavours.** In the terminology of the `openQ*D` code, a *quark flavour* is identified by all adjustable parameters that define the Dirac operator. For instance, in a simulation in the isospin symmetric limit, the up and down quark count as a single quark flavour. In the following example, two quark flavours are requested, and the parameters of the corresponding Dirac operators are initialized.

```
[Quark action]
nfl      2

[Flavour 0]          # Down quark
qhat     -2          # qhat must be integer
                     # el. charge = qhat/invqel = -2/6 = -1/3
kappa    0.136377    # hopping parameter
su3csw   1.909520    # ulcsw = su3csw = 0 => no O(a) improv.
ulcsw    1.0         # ulcsw = su3csw = 1 => tree-level O(a)
      improv.

[Flavour 1]          # Up quark
qhat     4           # el. charge = qhat/invqel = 4/6 = 2/3
kappa    0.137312
su3csw   1.909520
ulcsw    1.0
```

If different boundary conditions in time are chosen, the number of parameters in these sections increases, as one needs to specify the $O(a)$-improvement boundary coefficients. Also, if no C* boundary conditions are used, one can choose phase-periodic boundary conditions for fermions in space. Refer to `doc/dirac.pdf`, `doc/parms.pdf` for a detailed explanation of all these parameters.

7. **Rational approximation.** With C* boundary conditions, the Pfaffian of the even–odd preconditioned Dirac operator $\hat{D}$ is needed, whose absolute value can be generated by a pseudofermion effective action of the type $\psi^\dagger(\hat{D}^\dagger\hat{D})^{-1/4}\psi$. The fractional power of $\hat{D}^\dagger\hat{D}$ is replaced by a rational approximation, which must be generated by means of the `minmax` program [46,47]. We sketch here how to use this program, see `minmax/README` for more details.

First, one needs to modify the `GCC` and `MPLIBPATH` variables in `minmax/Makefile`. The Makefile assumes that the C compiler can be called by using `$(GCC)`, the GMP and MPFR header files are found in the `$(MPLIBPATH)/include/` directory, and the compiled libraries are found in the `$(MPLIBPATH)/lib/` directory.

```
22 GCC = gcc
23
24 MPLIBPATH = /usr/local
```

The `minmax` program is compiled and executed with the following commands in a bash shell.

```
cd ${HOME}/openQxD/minmax
make
./minmax -p -1 -q 4 -ra 1.98e-03
   -rb 7.62 -goal 6e-05
```

A rational approximation for $(\hat{D}^\dagger\hat{D})^\alpha$ is requested, with $\alpha = (-1)/(4)$ (`-p` and `-q` options), assuming that the eigenvalues of $(\hat{D}^\dagger\hat{D})^{1/2}$ are in the interval $[1.98 \times 10^{-3}, 7.62]$ (`-ra` and `-rb` options), with a target relative precision of 6×10^{-5} (`-goal` option). The spectral range of $(\hat{D}^\dagger\hat{D})^{1/2}$ must be guessed at first, but after some configurations have been generated it can be calculated with

the program `main/ms2`. The `minmax` program creates a directory with a very long name, in this case

```
p-1q4mu0.00000000e+00ra1.98000000e
  -03rb7.62000000e+00
```

which contains several files named `n*.in`. The integer in the file name corresponds to the order of the generated rational approximation. Only the highest order rational approximation, `n10.in` in this case, meets the requested precision. The full content of the `n10.in` must be pasted in the input file in a section of the following type,

```
[Rational 0]
power       -1 4
degree      10
range       1.98000000e-03 7.62000000e+00
mu          0.00000000e+00
delta       5.9691841082503071e-05
A           2.0497821359066373259 1e-01
nu[0]     1.2264797855989929331 6e+01
mu[0]     8.4073726152481462747 8e+00
# [...] the full content of n10.in must be pasted here
```

Notice that more than one rational approximation can be used in the same input file (e.g. one may want to use different rational approximations for the up, down and strange quarks). Each rational approximation is identified by the integer in the section title.

8. **MD Hamiltonian and integrator.**

```
[HMC parameters]
actions     0 1 2 3   # List of action IDs, see below
npf         2         # Number of pseudofermions to be allocated
nlv         2         # Number of levels of integrator for MD eqs
tau         2.0       # MD trajectory length
facc        1         # Fourier acceleration for U(1) MD
                      # (0 = not active, 1 = active)

[Level 0]             # Innermost level
integrator  OMF4      # Omelyan-Mryglod-Folk 4th order
nstep       2         # Number of times the elementary integrator
                      # is applied at this level
forces      0 1       # List of force IDs to be integrated at
                      # this level, see below

[Level 1]             # Outermost level
integrator  OMF4
nstep       1
forces      2 3
```

The MD Hamiltonian is given by the canonical kinetic term of the SU(3) gauge field, the kinetic term of the U(1) gauge field, and a sum of terms which do not depend on the MD momenta and are referred to as *actions*. The kinetic term of the U(1) gauge field can be chosen to be of two types: the canonical one (`facc=0`), or the Fourier-accelerated one (`facc=1`). Refer to `doc/fourier.pdf` and Sect. 2 for details on Fourier acceleration. The MD equations are solved by means of an approximate symplectic multilevel integrator, built in terms of standard elementary integrators. For each level, one needs to specify how many times the elementary integrator needs to be applied and which *forces* need to be integrated. Refer to `doc/parms.pdf` and `module/update/README.mdint` for details on the integrator.

The actions and forces are uniquely identified by an ID. Obviously there is a one-to-one correspondence between actions and forces. Corresponding actions and forces must share the same ID. The gauge actions and forces must be included, i.e.

```
[Action 0]            # No adjustable parameters here!
action      ACG_SU3

[Force 0]
force       FRG_SU3

[Action 1]
action      ACG_U1

[Force 1]
force       FRG_U1
```

In this example, two pseudofermion actions are used (notice that this number matches the number of pseudofermion fields requested in the `[HMC parameters]` section), one for *up* quark and one for the *down* quark.

```
[Action 2]
action  ACF_RAT_SDET # Rational approximation effective action
ipf     0            # Pseudofermion ID (a number from 0 to 1)
ifl     0            # Flavour ID (down quark)
irat    0 0 9        # Use the rational approximation with ID =
      0
                     # Include all rat. appr. factors, 0 -> 9,
                     # i.e. no frequency splitting
isp     0            # Solver ID, used to generate the p.f. at
                     # the beginning of the MD and to calculate
                     # the Hamiltonian at the end of the MD

[Force 2]
force   FRF_RAT_SDET
isp     1            # Solver ID, used to calculate the force

[Action 3]
action  ACF_RAT_SDET
ipf     1            # Different pseudofermion ID
ifl     1            # Different flavour ID (up quark)
irat    0 0 9
isp     0

[Force 3]
force   FRF_RAT_SDET
isp     1
```

Notice that `openQ*D` allows for frequency splitting (not used in this example): the poles and zeroes of the rational approximations can be separated in different pseudofermion actions. This is convenient because one may want to integrate different poles and zeroes in different levels of the integrator, and also one may want to use different solvers for different poles. For details on the pseudofermion actions and forces, and on the frequency splitting, one should refer to `doc/rhmc.pdf` and Sect. 2.

9. **Solvers.** Two multi-shift CG solvers are used in this example, with different residue for the actions and the forces.

```
[Solver 0]
solver      MSCG        # or CGNE, SAP_GCR, DFL_SAP_GCR
nmx         2048        # Maximum number of iterations
res         1.0e-11     # Residue

[Solver 1]
solver      MSCG
nmx         2048
res         1.0e-8
```

   For details on the usage of other solvers, one should refer to `doc/parms.pdf`. The deflated solver (`DFL_SAP_GCR`) requires to set parameters for the generation and update of the deflation subspaces, also described in `doc/parms.pdf`. See also Sect. 4.4.

10. **Wilson flow parameters.** The `iso1` program measures on the fly a number of simple observables (actions, SU(3) topological charge, electromagnetic fluxes) at positive flow time.

```
[Wilson flow]
integrator  RK3         # EULER: Euler, RK2: 2nd order
                        Runge-Kutta
                        # RK3: 3rd order Runge-Kutta
eps         2.0e-2      # Integration step size
nstep       700         # Total number of integration steps
dnms        5           # Number of steps between
                        measurements
```

4 Performance and testing

4.1 Code performance on parallel machines

For future reference and comparison, benchmark measurements have been performed for the timing of the application of the double precision Wilson–Dirac operator and the SAP (Schwartz-Alternating-Procedure) preconditioner. The HPC cluster at CERN has been used, which features 72 nodes, each of them with two 8-core Intel® Xeon processors (E5-2630 v3, Haswell) running at about 2.4 GHz base frequency (3.6 GHz max.). Nodes are connected with Mellanox® Infiniband FDR (56 Gb/s).

The timings are obtained with the `time2` programs located in the subdirectories `devel/dirac` and `devel/sap`. All measured times have been normalised to the smallest partition (one node or 16 cores). The results of these scaling tests are shown in Fig. 3. A QCD+QED setup with open boundary conditions in time and C* boundary conditions in one spatial direction has been used.

The weak scaling test has been performed with a local lattice size of $8 \times 16 \times 8 \times 8$, giving an extended lattice with total volume $V_{C^*} = 2N_{\mathrm{proc}}8^4$. Because of the C* boundary conditions this corresponds to a physical lattice with volume $V = N_{\mathrm{proc}}8^4$, cf. Sect. 2.1. While for the Dirac operator, parameters similar to the *Quark flavours* example (point 6) in Sect. 3.2 have been used, the SAP preconditioner specifically employs a block size of 4^4 with five SAP cycles (`ncy 5`) and five iterations (`nmr 5`) of the even–odd preconditioned Minimal Residue (MinRes) block solver. The setup is similar for the strong scaling study but with a constant total volume of $V_{C^*} = 2 \cdot 64 \times 32^3$ and varying local lattice sizes. In case of the double precision Wilson–Dirac operator, a much larger lattice volume with $V_{C^*} = 2 \cdot 64^4$ total lattice points was probed as well. As it can be seen in the left panel of Fig. 3 the larger lattice is performing even better than the smaller one.

In summary, the overall scaling studied here is close to optimal and small deviations may partly result from remaining indigestions of the underlying network. Similar studies have to be done on other machines but the overall behaviour is expected to be similar to the original `openQCD` code. Indeed, as already stressed, the `openQ*D` solvers are identical to the `openQCD` one. The Dirac operator is almost identical in the two codes, with the only difference that `openQ*D` uses the precalculated U(3) gauge field $Uz^{\hat{q}}$ instead of the SU(3) gauge field U. At fixed gauge background, the number of operations per lattice site performed by the Dirac operator is identical in the two codes, and so is the number of operations per lattice site per cycle performed by the solvers.

4.2 Low-level tests

The `openQ*D` code has been tested by means of an extensive battery of check programs, which can be found in the subdirectories of `devel`.[4] These programs have been taken over from `openQCD-1.6` and `NSPT-1.4`, and extended in order to test the specific feature of the `openQ*D` code. Roughly speaking, the check programs in each `devel` subdirectory test features of the corresponding `module` subdirectory. Many check programs test also interactions between different modules. These programs are meant to be used by developers only and contain very limited documentation. Providing a description of the check programs is outside of the scope of this paper, and a short description can be found in the `INDEX` files in each `devel` subdirectory. However, it is worth to point out a few facts. All check programs have been run with all possible combinations of boundary conditions in the space and temporal directions. Whenever possible, all check programs have been run in a pure QCD setup (i.e. only the SU(3) gauge field is allocated), a pure QED setup (i.e. only the U(1) gauge field is allocated), and a QCD+QED setup (i.e. both gauge fields are allocated). All check programs have been run with various geometric configurations,

[4] The `devel` directory contains 46,224 lines of code, against 60,203 lines of code in the `module` directory.

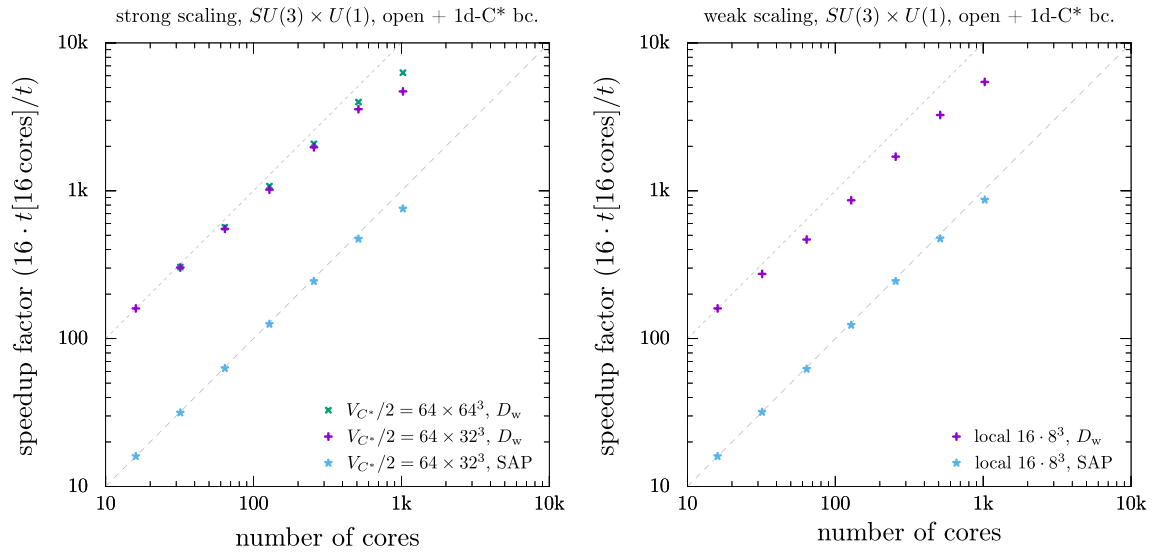

Fig. 3 Results for strong (left) and weak (right) scaling of the application of the Dirac operator and SAP preconditioner as explained in the text. The speedup factors for the Dirac operator are multiplied by a factor 10 for better visibility. The dashed lines indicate perfect scaling behaviour accordingly

i.e. lattice size and processor grid. Besides a plethora of minor details, specific check programs have been written to test:

- the implementation of C* boundary conditions for both gauge fields and for the Dirac operator;
- general properties of the Dirac operator with generic electric charge (e.g. gauge convariance, translational covariance, γ_5-hermiticity, comparison to analytic expression in case of zero gauge field);
- the rational approximation of generic powers, and the associated reweighting factors;
- the forces for the U(1) field, the QED action, the U(1) Wilson flow, the U(1) observables (e.g. clover field tensor, electromagnetic fluxes);
- the MD with the U(1) field, with and without Fourier acceleration.

4.3 Conservation of the Hamiltonian with Fourier acceleration

The use of Fourier Acceleration in QCD+QED simulations modifies the MD Hamiltonian and, consequently, the MD equations. In order to test the consistency between the two, one can look at the violation ΔH of Hamiltonian conservation as a function of the MD integration step-size $\Delta\tau$. The violation should vanish as a positive power of the integration step-size in the $\Delta\tau \to 0$ limit. The power depends on the chosen integrator. When the total trajectory length is kept constant, the leap-frog integrator (LF) and 2nd order Omelyan–Mryglod–Folk (OMF2) integrators yield $\Delta H \sim (\Delta\tau)^2$, while the 4th order Omelyan–Mryglod–Folk (OMF4) integrator yields $\Delta H \sim (\Delta\tau)^4$.

Figure 4 shows the violation ΔH as a function of $\Delta\tau$ for all integrators, with and without Fourier Acceleration. A two parameter function $\Delta H = a\,\Delta\tau^b$ has been fitted to the data points. In all cases the obtained exponent is reasonably close to the expected one. This test has been performed on a single thermalized configuration taken from the `Q*D1` ensemble (Table 1). As expected there is a clear hierarchy among the three integrators. More interestingly, Fourier Acceleration has the effect of reducing significantly ΔH. While no definite conclusion can be drawn from a single-configuration experiment in this regard, the same phenomenon has been observed in the generation of ensembles with the same parameters as the Q1 and Q2 runs described in [48], Table 2, with and without Fourier Acceleration: when Fourier Acceleration is turned on, if one wants to keep the acceptance rate the same, larger values of $\Delta\tau$ can be typically chosen. Obviously this does not mean that it is always convenient to use Fourier Acceleration. In order to understand whether this is the case, one should take into account the computational overhead and the variation in autocorrelations. Fourier acceleration is known to reduce significantly autocorrelations in the case of the free scalar theory, but also in the case of non-compact pure U(1) theory [11], which is a theory of free photons. However, in the experiments with the Q1 and Q2 ensembles discussed above, no significant difference could be detected in the autocorrelation times after thermalization. This may indicate that autocorrelations are unaffected by Fourier Acceleration in the interacting case. Substantiating this statement certainly requires a much more detailed study.

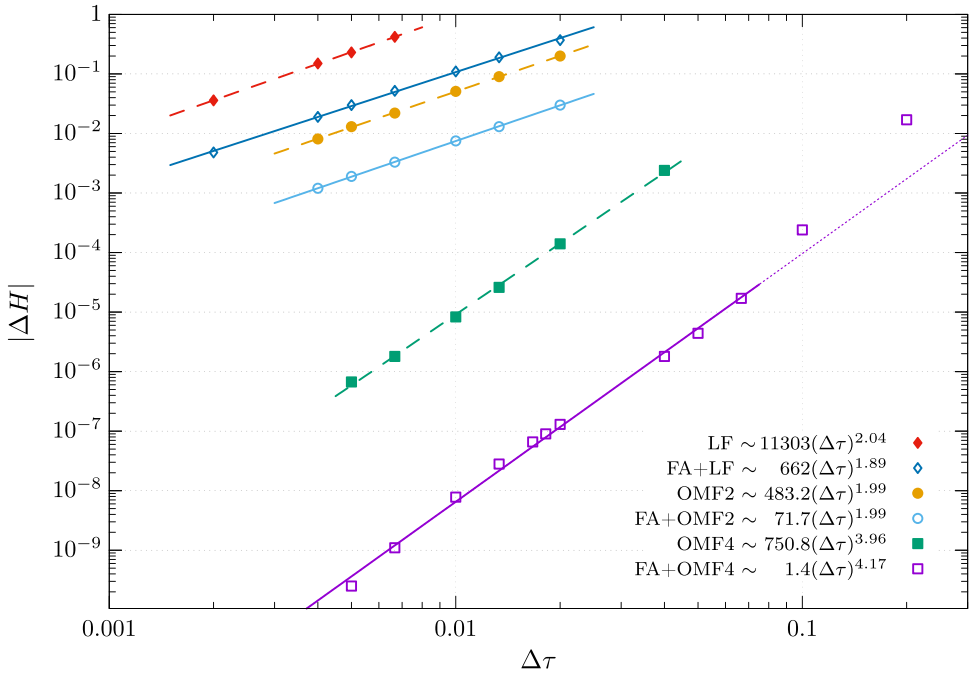

Fig. 4 Violations of MD Hamiltonian conservation ΔH as a function of the MD integration step-size $\Delta\tau$, for all available integrators (LF, OMF2, OMF4), with and without Fourier Acceleration (FA). The lines represent the fit functions provided in the legend

Table 1 Details of test runs employing C* boundary conditions in 3 spatial directions, and periodic boundary conditions in the temporal direction. Note that due to the C* boundary conditions, the global (simulated) lattice V_{C^*} is two times larger than the physical lattice because of the orbifold construction. $N_f = 3$ simulations of QCD+QED (`Q*D1`) use the tree-level improved Symanzik gauge action (LW) for the SU(3) gauge field with $c_{sw}^{SU(3)}$ taken from [49], and the Wilson plaquette action (W) for the electromagnetic field with $c_{sw}^{U(1)} = 1$. Furthermore, the electromagnetic coupling is set to $\alpha_0 = 0.05 \approx 7\alpha_0^{phys}$ with $q_{el} = 1/6$, i.e., the doublet $(d\ s)_{-1/3}$ and $(u)_{+2/3}$ have been simulated. The $N_f = 2$ pure QCD simulation (`QCD1`) uses the plaquette action with non-perturbative $c_{sw}^{SU(3)}$ of Ref. [50], and the lattice spacing was determined in Ref. [51]. All runs have degenerate quarks with hopping parameter κ. Values for the neutral pseudoscalar mass m_{PS} are given, as well as the flow time t_0/a^2 from which we naively derive the approximate lattice spacing of `Q*D1` using results of Ref. [52]. The number of simulated Molecular Dynamics Units (MDUs) after thermalization is reported in the last column. In both cases a MD trajectory length $\tau = 2$ has been used.

name	N_f	β	$V_{C^*}/2$	κ	t_0/a^2	a (fm)	m_{PS} (MeV)	MDUs
`QCD1`	2	5.3	64×32^3	0.136304	–	0.066	365	1300
`Q*D1`	2 + 1	3.55	32×16^3	0.137000	3.867(50)	0.074	660	1050

4.4 Performance of locally deflated solver in QCD+QED

The use of efficient solvers is a key factor in enabling simulations at quark masses close to the physical point. The `openQ*D` code inherits all the solvers of the `openQCD-1.6` package: Conjugate Gradient (CG), Multi-Shift Conjugate Gradient (MSCG), Generalized Conjugate Residual algorithm with Schwartz-Alternating-Procedure as preconditioning (SAP+GCR), and a deflated version of it (DFL+SAP+GCR). The deflated solver implements the idea of inexact deflation introduced in [22,53] and an improvement involving inaccurate projection in the deflation preconditioner proposed in [54].

As the Dirac operator is passed as an argument to these solvers, their implementation is blind to the coupling to the U(1) field and to C* boundary conditions. The efficiency of these solvers may be affected in principle by the coupling to the U(1) field, i.e. may depend on the electric charge of the Dirac operator. However this turns out not to be the case. The goal of this section is to describe two tests in support of this statement. These tests have been run on *Altamira* HPC at IFCA-CSIC, which consists of 158 computing nodes, each of them with two Intel® Xeon processors (E5-2670) at 2.6 GHz. Nodes are connected with Mellanox® Infiniband FDR (56 Gb/s).

An electroquenched (QCD+qQED) setup has been considered for both tests, with SU(3) configurations from the `QCD1` ensemble (Table 1) and pure U(1) configurations generated with $\alpha_0 = 0.05$ and $q_{el} = 1/6$. Two degenerate valence quarks Q and Q' have been considered, with electric charge q and bare mass m_0. The mass m_{PS} of the $\bar{Q}'\gamma_5 Q$ valence pseudoscalar neutral meson has been calculated as a function of q and m_0 and is shown in Fig. 5. Notice that the critical bare mass depends very heavily on the electric charge, as expected. For this reason it makes sense to compare

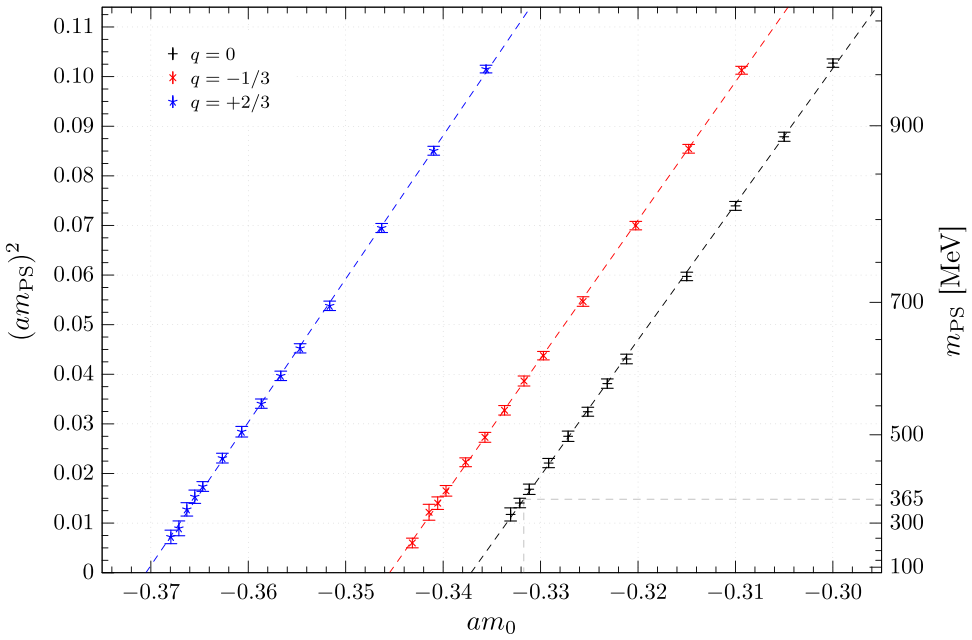

Fig. 5 Mass of the $\bar{Q}'\gamma_5 Q$ valence pseudoscalar neutral meson has been calculated as a function of q and $am_0 = 1/(2\kappa) - 4$. QCD + qQED setup: SU(3) configurations are taken from the `QCD1` ensemble (Table 1) and pure U(1) configurations are generated with $\alpha_0 = 0.05$ and $q_{\rm el} = 1/6$. The dashed curves are fits to the expected (leading order) quark mass dependence, $[m_{\rm PS}(q)]^2 = B(q)\{m_0 - m_{\rm cr}(q)\}$, and are shown only to guide the eye. The gray dashed line indicates the mass of the unitary point of the QCD simulation. In all cases, 50 gauge configurations separated by 26 MDUs have been used

the solver performance for different electric charges keeping fixed the value of $m_{\rm PS}$ (rather than the bare mass).

In the first test, the time needed to invert the even–odd preconditioned Dirac operator (with a representative QCD+qQED configuration) on 15 random sources has been measured, using the CG, SAP+GCR, and DFL+SAP+GCR solvers. The shortest time has been plotted in Fig. 6 for electric charges $q = 0, -1/3, 2/3$ and a range of values of $m_{\rm PS}$. It is evident that the performance of all solvers is insensitive to the electric charge.

One important caveat needs to be pointed out for the DFL+SAP+GCR solver. Before applying this solver, one needs to generate the deflation subspace, which is constructed from approximate eigenvectors of the Dirac operator. The code allows the possibility to choose different parameters for the Dirac operator used in the solver and the one used to generate the deflation subspace. This is very useful in practice since having a slightly heavier bare mass or even a twisted mass for the generation of the deflation subspace generally speeds up the calculation without affecting the performance of the solver. On the other hand, it is crucial to generate the deflation subspace with the same electric charge of the Dirac operator that needs to be inverted. If this is not done, the DFL+SAP+GCR solver loses efficiency dramatically. For this reason, in contrast to `openQCD-1.6`, the `openQ*D` code can handle simultaneously several deflation subspaces. These deflation subspaces can be generated with different parameters and will all be updated during the MD evolution. The user can specify in the input file which deflation subspace should be used for each DFL+SAP+GCR solver independently. In practice, in a realistic QCD+QED simulation, one would need to generate only two deflation subspaces, one for up-type quarks and one for down-type quarks. It has been checked also that the time needed to generate the deflation subspace is insensitive to the electric charge as long as $m_{\rm PS}$ is kept fixed.

In the second test, a single value of $m_{\rm PS} \simeq 354\,\text{MeV}$ has been chosen, and the time needed to invert $(\hat{D}^\dagger\hat{D} + \mu^2)$ has been measured for various values of the twisted mass μ, using the CG and DFL+SAP+GCR solvers. One representative QCD+qQED configuration and 48 random sources have been used. The shortest time has been plotted in Fig. 7 for electric charges $q = 0, -1/3, 2/3$ and a range of values of μ. The inversion of $(\hat{D}^\dagger\hat{D} + \mu^2)$ is relevant to calculate the rational approximation of non-integer powers of $\hat{D}^\dagger\hat{D}$ (see Sect. 2). Also in this case, the performance of the two solvers is seen to be insensitive to the electric charge as long as $m_{\rm PS}$ is kept fixed.

4.5 Key observables for HMC simulations of QCD+QED

Beside the electroquenched tests in the previous section, a new set of tests is done using dynamical QCD+QED simulations with Wilson fermions and C* boundary conditions.

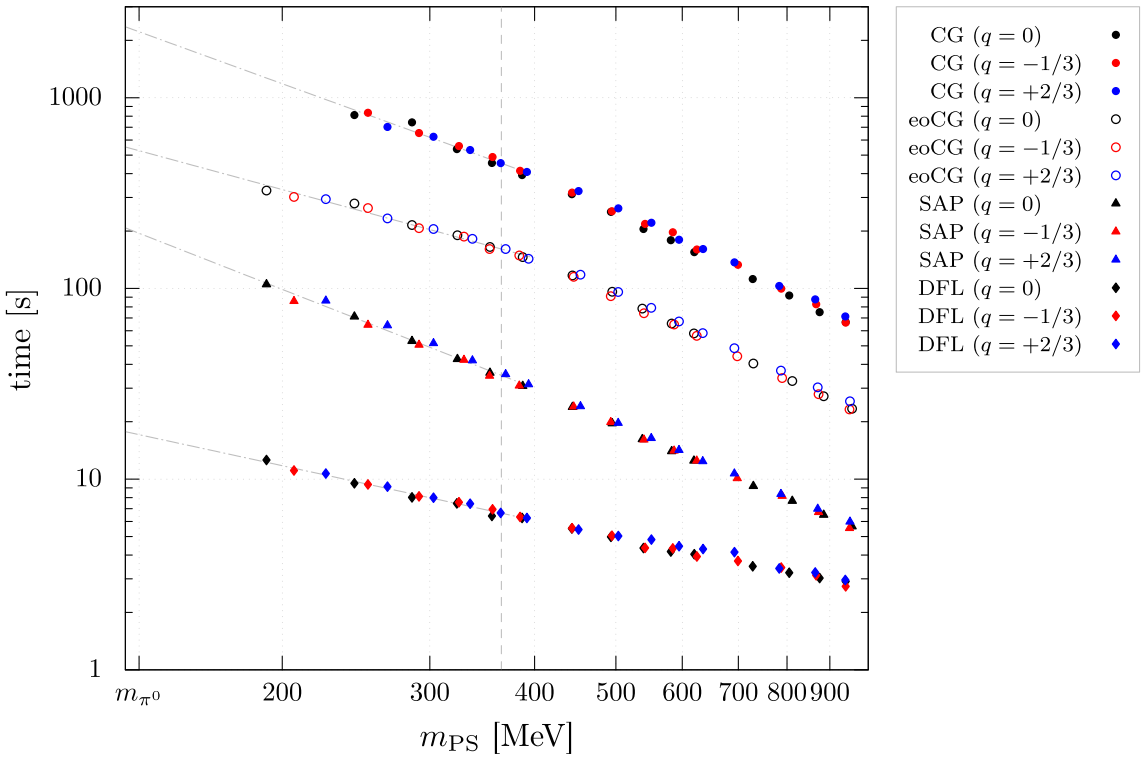

Fig. 6 Comparison of performance of various solvers and various electric charges as a function of the mass m_{PS} of the valence neutral pion. In all cases, the inverse of the even–odd preconditioned Dirac operator has been calculated on random sources. One representative QCD+qQED configuration has been used (SU(3) configuration from the `QCD1` ensemble, Table 1, and pure U(1) configuration generated with $\alpha_0 = 0.05$ and $q_{\mathrm{el}} = 1/6$). The same residue of 10^{-10} has been chosen for the three solvers. The solver performance is insensitive to the electric charge

The dynamical degrees of freedom of the U(1) gauge field are included in the simulation labeled `Q*D1` in Table 1. `Q*D1` takes over the parameters from the H200 ensemble of the $N_{\mathrm{f}} = 2 + 1$ CLS [55] effort, except that the lattice extent is halved in each of the space-time directions. As the dynamical U(1) degrees of freedom contribute to the renormalization of the bare parameters, the estimate for the lattice spacing and pion mass cannot be taken over from the CLS ensembles,[5] but rather need to be estimated independently. Such an endeavour is beyond the scope of this paper. However, an estimate for t_0/a^2 is given in Table 1 for future reference. The reference flow time t_0 is implicitly given by $[t_0^2\langle E(t_0)\rangle] = 0.3$ using the Wilson flow and clover discretisation of the SU(3) field strength tensor in the definition of the energy density $E(t)$ [56]. A rough estimate of a is given after naively matching t_0/a^2 to the data provided in Table III of Ref. [52].

Although `openQ*D` allows for twisted-mass reweighting, that option is not required for `Q*D1` ($\mu = 0.0$). All three bare sea quark masses, $am_{0,i} = 1/(2\kappa_i) - 4$, are taken to be degenerate. As demonstrated in the previous section and shown in Fig. 5, this necessarily leads to a large difference in the neutral pseudoscalar masses due to the differences in quark charges. One thus ends up with a degenerate pair of down-type quarks ($q = -1/3$), and a single but significantly heavier up-type quark ($q = 2/3$). Hence, the simulations are essentially probing a somewhat unphysical version of the $N_{\mathrm{f}} = 2 + 1$ theory, but are sufficient to probe standard observables and performance of the code.

In Fig. 8 a summary of selected observables is given for simulation `Q*D1`. The run was stable and did not show any particular issue during the course of the simulation. Most of the observables presented in the following include the thermalisation part. Starting from a random configuration, the HMC energy violations, measured every trajectory ($\tau = 0.7$ MDU), drop after a few iterations and stably fluctuate in the range $[-0.5, +0.5]$. The simulation employs the OMF4 integrator without Fourier acceleration and the spectral ranges of the individual quark flavours have been properly set. Next the average plaquette for the SU(3) and U(1) gauge fields are presented. The former is shifted by a constant amount for better comparison. The SU(3) plaquette has much larger statistical fluctuations and requires longer thermalisation times than the U(1) plaquette even without Fourier acceleration. The next two plots show the two avail-

[5] Had the U(1) d.o.f. been switched off ($\alpha_0 = 0$), the chosen parameter set would correspond to $a \approx 0.064$ fm and $m_{\mathrm{PS}} \approx 420$ MeV.

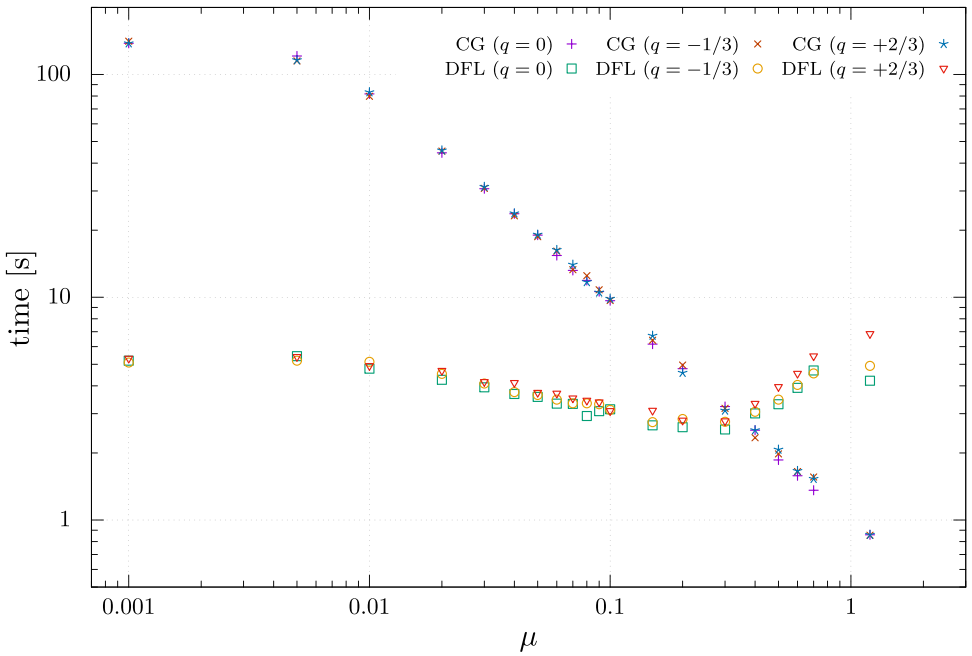

Fig. 7 Comparison of performance of various solvers and various electric charges as a function of the twisted mass μ. In all cases, the inverse of $(\hat{D}^\dagger \hat{D} + \mu^2)$ has been calculated on random sources. The mass of the valence neutral pion (calculated at $\mu = 0$) has been chosen to be $m_{\rm PS} \simeq 329\,\text{MeV}$. One representative QCD+qQED configuration has been used (SU(3) configuration from the `QCD1` ensemble, Table 1, and pure U(1) configuration generated with $\alpha_0 = 0.05$ and $q_{\rm el} = 1/6$). The same residue of 10^{-8} has been chosen for the three solvers. The solver performance is insensitive to the electric charge. As expected, the deflated solver loses efficiency at large values of μ and eventually fails to converge for the three highest value

able definitions of the (renormalized) energy density $E(t)$ at a flow time $t = 3.2$ for the SU(3) and U(1) part, respectively. The topological charge Q (measured at the same flow time) fluctuates well after rapid changes during the thermalisation phase of the run. The smallest eigenvalues of $|\gamma_5 \hat{D}_{\rm u}|$ and $|\gamma_5 \hat{D}_{\rm d/s}|$ follow, confirming that the lower end of the spectral ranges of the rational approximations have been chosen correctly. No exceptionally small values are present, which is not surprising considering the heavy pseudoscalar mass simulated here.

The `Q*D1` run has been produced with a rational approximation with relative precision $\delta = O(10^{-11})$. A second run has been performed with the same parameters as `Q*D1` except for the rational approximation, which has been chosen with relative precision $\delta = O(10^{-9})$. The logarithms of the reweighing factors for both runs are shown in the last two panes of Fig. 8. As expected, the reweighting factor for the run with a better rational approximation is closer to 1 (and its logarithm is closer to 0).

5 Summary and outlook

We presented `openQ*D` [1], the first open source package which allows to perform full lattice simulations of QCD+QED, QCD or QED. The code implements the proposal of Ref. [18] and allows to choose C* boundary conditions along the spatial directions but also periodic boundary conditions can be simulated efficiently. Moreover, the chosen theory can be simulated by choosing either periodic, Schrödinger Functional or open boundary conditions along the time direction.

The new code is based on the `openQCD` [2] package from which it inherits the highly optimized implementation of the Dirac operator, of the solvers, of the HMC and of the RHMC algorithms. The `openQ*D` package extends the algorithmic functionalities of the `openQCD` code by giving the possibility of using multiple deflation subspaces in a single simulation, of implementing rational approximations of generic powers of the Dirac operator (with and without twisted-mass preconditioning) and by implementing Fourier Acceleration for the evolution of the U(1) field.

We presented the main functionalities of the code and discussed the theoretical motivations behind the algorithmic choices and their specific implementations. We also presented a guide to instruct the user to run a full QCD+QED simulation with `openQ*D` and discussed the results of some tests. These include low-level tests aiming at assessing the correctness of the implementation of the different algorithms but also some benchmarks to measure the performance of the code.

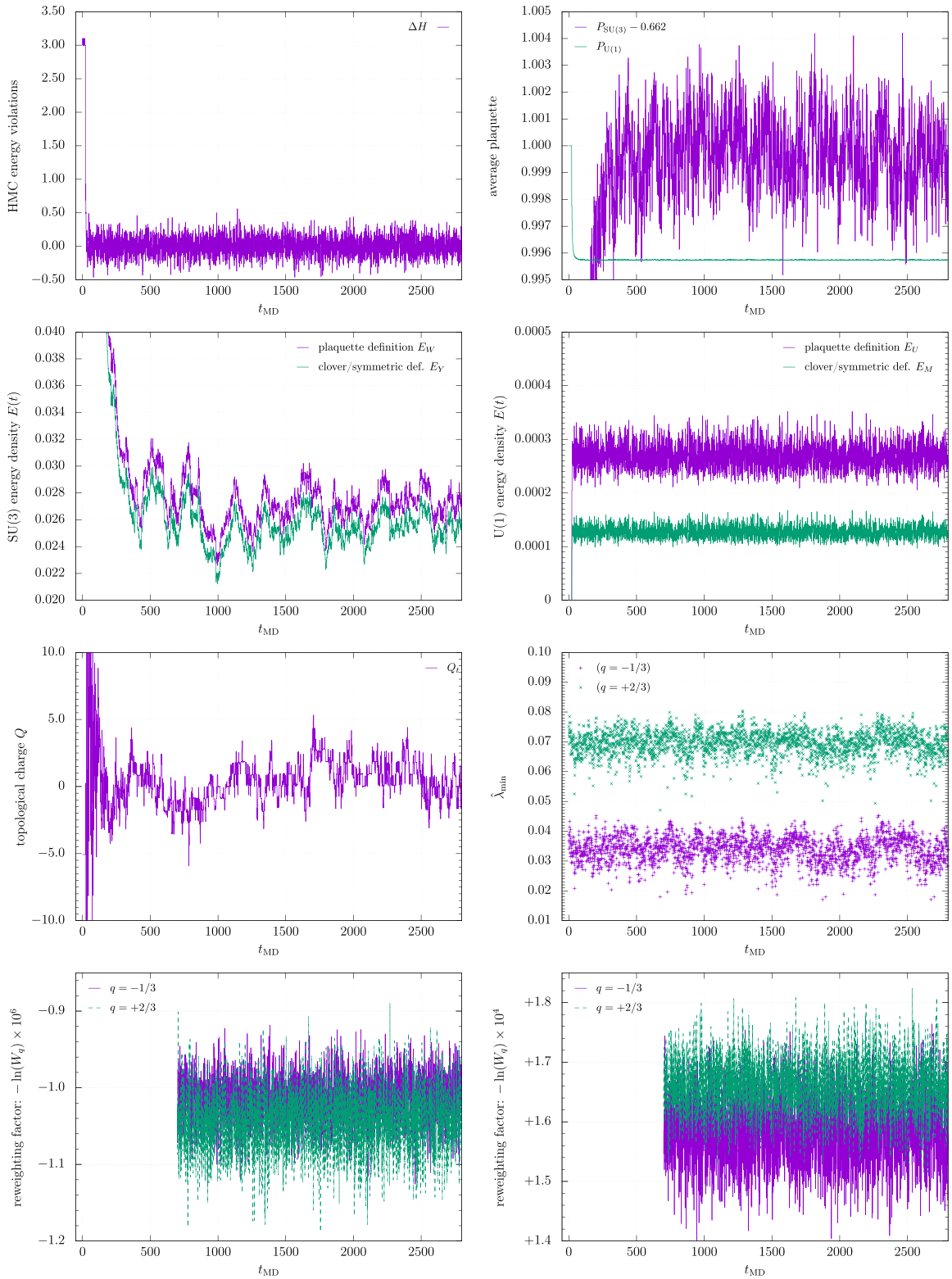

Fig. 8 Selected observables for simulation `Q*D1` including thermalisation part. Left–right/top–bottom: HMC energy violations ΔH, average plaquette for SU(3) and U(1) gauge fields, energy density $E(t)$ for SU(3), energy density for U(1), topological charge $Q(t)$, lowest eigenvalue $\hat{\lambda}_{\mathrm{min}}$ in the spectrum of $|\gamma_5 \hat{D}|$, and reweighting factors W_q for two different numerical accuracies, $\delta = O(10^{-11})$ (left) and $\delta = O(10^{-9})$ (right)

In future releases we plan to add a number of features. Concerning the configuration generation, we will include the possibility to use a gauge-fixed non-compact formulation of QED. We will also provide programs to calculate a number of observables, in particular charged-meson two-point functions with QED dressing-factors along the lines of [18], and quark gradient flow observables [57]. Finally we will consider incorporating some of the algorithmic developments discussed in [58], in particular stabilized Wilson fermions.

Given the good performance and high scalability on modern supercomputing cluster architectures, `openQ*D` can profitably be used to generate QCD+QED gauge configurations with C* boundary conditions (but not only) in a realistic setup with the aim of computing QED radiative corrections to phenomenologically relevant observables.

Acknowledgements The simulations were performed on the following HPC systems: Altamira, provided by IFCA at the University of Cantabria; FinisTerrae II, provided by CESGA (Galicia Supercomputing Centre); the Lonsdale cluster maintained by the Trinity Centre for High Performance Computing; and the Lattice-HPC cluster at CERN. FinisTerrae II was funded by the Xunta de Galicia and the Spanish MINECO under the 2007–2013 Spanish ERDF. Lonsdale was funded through grants from the Science Foundation Ireland. We thankfully acknowledge the computer resources offered and the technical support provided by the staff of these computing centers. We thank the Theoretical Physics Department at CERN for hospitality during the workshop *Advances in Lattice Gauge Theory 2019*, allowing us to jointly finalise the present work.

Data Availability Statement This manuscript has associated data in a data repository. [Authors' comment: All presented data sets can be easily generated using openQ*D [1].]

Open Access This article is licensed under a Creative Commons Attribution 4.0 International License, which permits use, sharing, adaptation, distribution and reproduction in any medium or format, as long as you give appropriate credit to the original author(s) and the source, provide a link to the Creative Commons licence, and indicate if changes were made. The images or other third party material in this article are included in the article's Creative Commons licence, unless indicated otherwise in a credit line to the material. If material is not included in the article's Creative Commons licence and your intended use is not permitted by statutory regulation or exceeds the permitted use, you will need to obtain permission directly from the copyright holder. To view a copy of this licence, visit http://creativecommons.org/licenses/by/4.0/.
Funded by SCOAP[3].

A Implementation of the RHMC

A.1 Rational approximation

It is convenient to introduce the hermitian operator $\hat{Q} = \gamma_5 \hat{D}$, in terms of which $\hat{D}^\dagger \hat{D} = \hat{Q}^2$. Assume that the spectrum of $|\hat{Q}|$ is contained in the interval $[r_a, r_b]$, and choose an integer n. A rational function of order $[n, n]$ in q^2 has the form

$$\rho(q^2) = A \prod_{j=1}^{n} \frac{q^2 + \nu_j^2}{q^2 + \mu_j^2}. \tag{A.1}$$

Without loss of generality one can assume

$$\nu_1 > \nu_2 > \cdots > \nu_n, \quad \mu_1 > \mu_2 > \cdots > \mu_n. \tag{A.2}$$

$\rho(q^2)$ is chosen to be the optimal rational approximation of order $[n, n]$ of the function $(q^2 + \hat{\mu}^2)^{-\alpha}$ in the domain $q \in [r_a, r_b]$, i.e. the rational function of the form (A.1) which minimizes the uniform relative error

$$\delta = \max_{q \in [r_a, r_b]} |1 - (q^2 + \hat{\mu}^2)^\alpha \rho(q^2)|. \tag{A.3}$$

As explained in Sect. 3.2.2, the optimal rational approximation can be calculated with the `minmax` code which implements the minmax approximation algorithm in multiple precision.

If $\rho(q^2)$ is the desired optimal rational approximation, the operator R which appears in Eq. (2.6) is defined simply as

$$R = \rho(\hat{Q}^2) = \rho(\hat{D}^\dagger \hat{D}) = A \prod_{j=1}^{n} \frac{\hat{D}^\dagger \hat{D} + \nu_j^2}{\hat{D}^\dagger \hat{D} + \mu_j^2}. \tag{A.4}$$

Equation (A.3) implies the following norm bound

$$\|1 - (\hat{D}^\dagger \hat{D} + \hat{\mu}^2)^\alpha R\| \le \delta. \tag{A.5}$$

A.2 Frequency splitting and pseudofermion action

`openQ*D` inherits from `openQCD` the frequency splitting of the rational approximation: the factors of the rational approximation can be split in different pseudofermion actions; the corresponding forces can be included in different levels of the MD integrator, providing a useful handle to optimize the algorithm. This procedure is similar to the Hasenbusch decomposition for the HMC algorithm [59].

The rational approximation constructed in Sect. A.1 is broken up in factors of the form

$$P_{k,l} = \prod_{j=k}^{l} \frac{\hat{D}^\dagger \hat{D} + \nu_j^2}{\hat{D}^\dagger \hat{D} + \mu_j^2}. \tag{A.6}$$

For example, if $n = 12$ a possible factorization is

$$R = A P_{1,5} P_{6,9} P_{10,12}. \tag{A.7}$$

The contribution of R to the quark determinant is

$$\det R^{-1} = \text{constant} \times \det P_{1,5}^{-1} \ \det P_{6,9}^{-1} \ \det P_{10,12}^{-1}. \tag{A.8}$$

Each $P_{k,l}^{-1}$ determinant is simulated as usual by adding a pseudofermion action of the form

$$S_{\mathrm{pf},k,l} = (\phi_{\mathrm{e}}^{k,l},\, P_{k,l} \phi_{\mathrm{e}}^{k,l}), \tag{A.9}$$

where the fields $\phi_{\rm e}^{k,l}$ are independent pseudofermions that live on the even sites of the lattice. By using a partial fraction decomposition

$$P_{k,l} = 1 + \sum_{j=k}^{l} \frac{\sigma_j}{\hat{D}^\dagger \hat{D} + \mu_j^2}, \tag{A.10}$$

$$\sigma_j = (\nu_j^2 - \mu_j^2) \prod_{\substack{m=l,\ldots,k \\ m\neq j}} \frac{\nu_m^2 - \mu_j^2}{\mu_m^2 - \mu_j^2}, \tag{A.11}$$

the pseudofermion action in Eq. (A.9) is cast into a sum of terms of the type

$$S_{{\rm pf},k,l} = (\phi_{\rm e}^{k,l}, \phi_{\rm e}^{k,l}) + \sum_{j=k}^{l} \sigma_j \, (\phi_{\rm e}^{k,l}, (\hat{D}^\dagger \hat{D} + \mu_j^2)^{-1} \phi_{\rm e}^{k,l}). \tag{A.12}$$

A.3 Reweighting factors

Let $\tilde{R}$ and R be the optimal rational approximations of order $[n,n]$ for $(\hat{D}^\dagger \hat{D})^{-\alpha}$ and $(\hat{D}^\dagger \hat{D} + \hat{\mu}^2)^{-\alpha}$ respectively. It is assumed that the relative errors of the two rational approximations are not greater than δ in the common spectral range $[r_a, r_b]$.

The reweighting factor W defined in Eq. (2.8) is decomposed in two factors which are calculated separately, i.e.

$$W = W_{\rm rat} W_{\rm rtm}, \tag{A.13}$$

$$W_{\rm rat} = \det[(\hat{D}^\dagger \hat{D})^\alpha \tilde{R}], \tag{A.14}$$

$$W_{\rm rtm} = \det[\tilde{R}^{-1} R]. \tag{A.15}$$

A.3.1 Reweighting factor W_{rat}

In the calculation of the reweighting factor $W_{\rm rat}$ in Eq. (A.14), it is assumed that the exponent α is a positive rational number of the form

$$\alpha = \frac{u}{v}, \tag{A.16}$$

where u and v are natural numbers. The reweighting factor can be represented as

$$W_{\rm rat} = \det[\hat{Q}^{2u} \tilde{R}^v]^{\frac{1}{v}} = \det(1+Z)^{\frac{1}{v}}, \tag{A.17}$$

where the operator Z is defined as

$$Z = \hat{Q}^{2u} \tilde{R}^v - 1. \tag{A.18}$$

The determinant in Eq. (A.17) is estimated stochastically

$$W_{\rm rat} = \lim_{N\to\infty} \frac{1}{N} \sum_{j=1}^{N} \exp\{-(\eta_{\rm e}^j, [(1+Z)^{-\frac{1}{v}} - 1]\eta_{\rm e}^j)\}, \tag{A.19}$$

where the fields $\eta_{\rm e}^j$ are N independent normally-distributed pseudofermions that live on the even sites of the lattice. From the norm bound in Eq. (A.5) for $\hat{\mu} = 0$, and the positivity of $\tilde{R}$ (which is guaranteed if the relative error δ is small enough), it follows that

$$0 \le 1 + Z = \hat{Q}^{2u} \tilde{R}^v = [\hat{Q}^{2\alpha} \tilde{R}]^v \le (1+\delta)^v, \tag{A.20}$$

which yields the norm bound

$$\|Z\| \le \Delta = (1+\delta)^v - 1 = v\delta + O(\delta^2). \tag{A.21}$$

Therefore the Taylor series

$$(1+Z)^{-\frac{1}{v}} = 1 + \sum_{n=1}^{\infty} c_{v,n} \, Z^n,$$
$$c_{v,n} = (-1)^n \frac{\frac{1}{v}\left(\frac{1}{v}+1\right)\cdots\left(\frac{1}{v}+n-1\right)}{n!}, \tag{A.22}$$

converges rapidly in operator norm. The exponent in Eq. (A.19) can be estimated from the first few terms of

$$(\eta_{\rm e}^j, [(1+Z)^{-\frac{1}{v}} - 1]\eta_{\rm e}^j) = \sum_{n=1}^{\infty} c_{v,n} \, (\eta_{\rm e}^j, Z^n \eta_{\rm e}^j). \tag{A.23}$$

It is possible to estimate the size of these terms by noting that $\|\eta_{\rm e}^j\|^2$ is very nearly equal to 12 times the number $N_{\rm e}$ of even lattice points. Taking the bound (A.21) into account, the following estimate is obtained

$$|(\eta_{\rm e}^j, Z^n \eta_{\rm e}^j)| \le \|Z\|^n \, \|\eta_{\rm e}^j\|^2 \le \Delta^n \|\eta_{\rm e}^j\|^2 \simeq 12(v\delta)^n N_{\rm e}. \tag{A.24}$$

The statistical fluctuations of the exponents in Eq. (A.19) derive from those of the gauge field and those of the random sources $\eta_{\rm e}^j$. For a given gauge field, the variance of the exponent is equal to

$$\begin{aligned} {\rm tr}\,\{[(1+Z)^{-\frac{1}{v}} - 1]^2\} &= \frac{1}{v^2} {\rm tr}\, Z^2 + O(\delta^3) \\ &\le 12 N_{\rm e} \delta^2 + O(\delta^3). \end{aligned} \tag{A.25}$$

These fluctuations are guaranteed to be small if, for instance, $12N_{\rm e}\delta^2 \le 10^{-4}$. One can then just as well set $N = 1$ in Eq. (A.19), i.e. a sufficiently accurate stochastic estimate of $W_{\rm rat}$ is obtained in this case with a single random source.

When the stronger constraint $12N_{\rm e}\delta \le 10^{-2}$ is satisfied, the reweighting factor $W_{\rm rat}$ deviates from 1 by at most 1%. Larger approximation errors can however be tolerated in practice as long as the fluctuations of $W_{\rm rat}$ remain small.

A.3.2 Reweighting factor $W_{\rm rtm}$

Let us choose a rational approximation R of order $[n, n]$ for $(\hat{D}^\dagger \hat{D} + \hat{\mu}^2)^{-\alpha}$ of the form

$$R = A \prod_{j=1}^{n} \frac{\hat{D}^\dagger \hat{D} + \nu_j^2}{\hat{D}^\dagger \hat{D} + \mu_j^2}, \tag{A.26}$$

$$\nu_1 > \nu_2 > \cdots > \nu_n, \quad \mu_1 > \mu_2 > \cdots > \mu_n, \tag{A.27}$$

and a rational approximation $\tilde{R}$ of order $[n, n]$ for $(\hat{D}^\dagger \hat{D})^{-\alpha}$ of the form

$$\tilde{R} = \tilde{A} \prod_{j=1}^{n} \frac{\hat{D}^\dagger \hat{D} + \tilde{\nu}_j^2}{\hat{D}^\dagger \hat{D} + \tilde{\mu}_j^2}, \tag{A.28}$$

$$\tilde{\nu}_1 > \tilde{\nu}_2 > \cdots > \tilde{\nu}_n, \quad \tilde{\mu}_1 > \tilde{\mu}_2 > \cdots > \tilde{\mu}_n. \tag{A.29}$$

Let us rewrite Eq. (A.15) as

$$W_{\rm rtm} = \det[R^{-1}\tilde{R}]^{-1}. \tag{A.30}$$

Notice that the operator $R^{-1}\tilde{R}$ is also a rational function of $\hat{Q}^2 = \hat{D}^\dagger \hat{D}$. It is convenient to break up this rational function in factors of the type

$$\tilde{P}_{k,l} = \prod_{j=k}^{l} \frac{(\hat{D}^\dagger \hat{D} + \mu_j^2)(\hat{D}^\dagger \hat{D} + \tilde{\nu}_j^2)}{(\hat{D}^\dagger \hat{D} + \nu_j^2)(\hat{D}^\dagger \hat{D} + \tilde{\mu}_j^2)}. \tag{A.31}$$

If $n = 12$, for example, the reweighting factor $W_{\rm rtm}$ can be factorized as

$$W_{\rm rtm} = \text{constant} \times \det \tilde{P}_{1,5}^{-1} \ \det \tilde{P}_{6,9}^{-1} \ \det \tilde{P}_{10,12}^{-1}. \tag{A.32}$$

Each of the above determinants is estimated stochastically

$$\det \tilde{P}_{k,l}^{-1} = \lim_{N\to\infty} \frac{1}{N} \sum_{j=1}^{N} \exp\{-(\eta_{\rm e}^j, [\tilde{P}_{k,l} - 1]\eta_{\rm e}^j)\}, \tag{A.33}$$

where the fields $\eta_{\rm e}^j$ are N independent normally-distributed pseudofermions that live on the even sites of the lattice. It is useful to consider the partial fraction decomposition

$$\tilde{P}_{k,l} = 1 + \sum_{j=k}^{l} \left(\frac{\sigma_j}{\hat{D}^\dagger \hat{D} + \nu_j^2} + \frac{\tilde{\sigma}_j}{\hat{D}^\dagger \hat{D} + \tilde{\mu}_j^2} \right), \tag{A.34}$$

$$\sigma_j = \frac{(\tilde{\nu}_j^2 - \nu_j^2)(\mu_j^2 - \nu_j^2)}{\tilde{\mu}_j^2 - \nu_j^2} \prod_{\substack{m=l,\ldots,k \\ m\neq j}} \frac{(\tilde{\nu}_m^2 - \nu_j^2)(\mu_m^2 - \nu_j^2)}{(\tilde{\mu}_m^2 - \nu_j^2)(\nu_m^2 - \nu_j^2)}, \tag{A.35}$$

$$\tilde{\sigma}_j = \frac{(\tilde{\nu}_j^2 - \tilde{\mu}_j^2)(\mu_j^2 - \tilde{\mu}_j^2)}{\nu_j^2 - \tilde{\mu}_j^2} \prod_{\substack{m=l,\ldots,k \\ m\neq j}} \frac{(\tilde{\nu}_m^2 - \tilde{\mu}_j^2)(\mu_m^2 - \tilde{\mu}_j^2)}{(\tilde{\mu}_m^2 - \tilde{\mu}_j^2)(\nu_m^2 - \tilde{\mu}_j^2)}. \tag{A.36}$$

Typically σ_j and $\tilde{\sigma}_j$ are found to have opposite signs. Also, for small values of j, $|\sigma_j|$ and $|\tilde{\sigma}_j|$ are of the same order of magnitude, therefore it is convenient for numerical stability to use the following representation

$$\tilde{P}_{k,l} = 1 + \sum_{j=k}^{l} \frac{(\sigma_j + \tilde{\sigma}_j)(\hat{D}^\dagger \hat{D}) + \sigma_j \tilde{\mu}_j^2 + \tilde{\sigma}_j \nu_j^2}{(\hat{D}^\dagger \hat{D} + \nu_j^2)(\hat{D}^\dagger \hat{D} + \tilde{\mu}_j^2)}. \tag{A.37}$$

B Laplacian for the Fourier accelerated molecular dynamics

The U(1) momentum is generally represented in momentum space as

$$\pi(x, \mu) = \frac{1}{L^3} \sum_{p_0 \in E_\mu} \sum_{\mathbf{p}\in\mathcal{P}} e_\mu(p_0, x_0) e^{i\mathbf{px}} \tilde{\pi}(p, \mu). \tag{B.1}$$

The basis functions $e_\mu(p_0, x_0)$ (for fixed μ) are orthogonal with respect to a weighted scalar product

$$\sum_{x_0} w_\mu(x_0) e_\mu^*(p_0, x_0) e_\mu(q_0, x_0) = \delta_{p_0,q_0}, \tag{B.2}$$

where the weight $w_\mu(x)$ is taken to be $1/2$ if x belongs to an open boundary (i.e. $x_0 = 0$ for open and open-SF b.c.s, and $x_0 = T - 1$ for open b.c.s) and $\mu = 1, 2, 3$. In all other cases $w_\mu(x)$ is taken to be 1. The relation between π and $\tilde{\pi}$ is easily inverted

$$\tilde{\pi}(p, \mu) = \sum_{x} w_\mu(x_0) e_\mu^*(p_0, x_0) e^{-i\mathbf{px}} \pi(x, \mu). \tag{B.3}$$

The set $\mathcal{P}$ is given by all spatial momenta $\mathbf{p} = (p_1, p_2, p_3)$ of the form

$$p_k = \tfrac{\pi}{L_k}(2n_k + c_k) \quad \text{with } n_k = 0, \ldots, L_k - 1, \tag{B.4}$$

where $c_k = 0$ if k is a periodic direction and $c_k = 1$ if k is a C* direction. The sets E_μ and the eigenfunctions $e_\mu(p_0, x_0)$ depend on the boundary conditions in time. In the following $k = 1, 2, 3$.

- Open boundary conditions:

$$E_0 = \frac{\pi}{N_0 - 1}\{1, \ldots, N_0 - 1\},$$
$$E_k = \frac{\pi}{N_0 - 1}\{0, \ldots, N_0 - 1\}, \tag{B.5}$$
$$e_0(p_0, x_0) = \frac{i}{(1 + \delta_{p_0,\pi})(N_0 - 1)} \sin\left[p_0 \left(x_0 + \frac{1}{2} \right) \right], \tag{B.6}$$
$$e_k(p_0, x_0) = \frac{1}{(1 + \delta_{p_0,0} + \delta_{p_0,\pi})(N_0 - 1)} \cos(p_0 x_0). \tag{B.7}$$

- SF boundary conditions:

$$E_0 = \frac{\pi}{N_0}\{0, \ldots, N_0 - 1\},$$
$$E_k = \frac{\pi}{N_0}\{1, \ldots, N_0 - 1\}, \tag{B.8}$$
$$e_0(p_0, x_0) = \frac{1}{(1+\delta_{p_0,\pi})N_0} \cos\left[p_0\left(x_0 + \frac{1}{2}\right)\right], \tag{B.9}$$
$$e_k(p_0, x_0) = \frac{i}{N_0} \sin(p_0 x_0). \tag{B.10}$$

- Open-SF boundary conditions:

$$E_0 = E_k = \frac{\pi}{N_0}\left(\{0, \ldots, N_0 - 1\} + \frac{1}{2}\right), \tag{B.11}$$
$$e_0(p_0, x_0) = \frac{i}{N_0} \sin\left[p_0\left(x_0 + \frac{1}{2}\right)\right], \tag{B.12}$$
$$e_k(p_0, x_0) = \frac{1}{N_0} \cos\left[p_0\left(x_0 + \frac{1}{2}\right)\right]. \tag{B.13}$$

- Periodic boundary conditions:

$$E_0 = E_k = \frac{2\pi}{N_0}\{0, \ldots, N_0 - 1\}, \tag{B.14}$$
$$e_0(p_0, x_0) = e_k(p_0, x_0) = \frac{1}{N_0} \exp(i p_0 x_0). \tag{B.15}$$

We use the Fourier decomposition to define the intermediate operator D_{N}

$$[D_{\mathrm{N}}\pi](x, \mu) = \frac{1}{L^3} \sum_{p_0 \in E_\mu} \sum_{\mathbf{p} \in \mathcal{P}} e_\mu(p_0, x_0) e^{i\mathbf{p}\mathbf{x}} \tilde{D}_{\mathrm{N}}(p) \tilde{\pi}(p, \mu), \tag{B.16}$$

$$\tilde{D}_{\mathrm{N}}(p) = \begin{cases} 1 & \text{if } p = 0 \\ 4\sum_\mu \sin^2 \frac{p_\mu}{2} & \text{otherwise.} \end{cases} \tag{B.17}$$

Explicity

$$D_{\mathrm{N}}(x, \mu; y, \nu) = \frac{1}{L^3} \sum_{p_0 \in E_\mu} \sum_{\mathbf{p} \in \mathcal{P}} \tilde{D}_{\mathrm{N}}(p) \delta_{\mu\nu} e^{i\mathbf{p}(\mathbf{x}-\mathbf{y})} e_\mu(p_0, x_0) e^*_\nu(p_0, y_0) w_\nu(y_0). \tag{B.18}$$

With respect to the scalar product defined by

$$(\phi, \phi)_G = (\phi, G\phi), \tag{B.19}$$
$$[G\phi](x, \mu) = w_\mu(x_0)\phi(x, \mu). \tag{B.20}$$

the operator D_{N} is symmetric and strictly positive, i.e.

$$(\phi', D_{\mathrm{N}}\phi)_G = (D_{\mathrm{N}}\phi', \phi)_G, \tag{B.21}$$
$$(\phi, D_{\mathrm{N}}\phi)_G \geq 0, \tag{B.22}$$
$$(\phi, D_{\mathrm{N}}\phi)_G = 0 \Leftrightarrow \phi = 0. \tag{B.23}$$

The desired operator is defined as

$$\Delta = G^{1/2} D_{\mathrm{N}} G^{-1/2}. \tag{B.24}$$

Symmetry and strict positivity of Δ with respect to the canonical scalar product of Δ follow from the corresponding properties of D_{N}. Notice that

$$D^\alpha = G^{1/2} D^\alpha_{\mathrm{N}} G^{-1/2}. \tag{B.25}$$

The `openQ*D` code uses the Fast Fourier Transform (FFT) algorithm to construct $\tilde{\pi}(p, \mu)$ from $\pi(x, \mu)$ and vice versa. The FFT is implemented in the module `dft` which is an adaptation of the corresponding module in the `NSPT-1.4` code written by Mattia Dalla Brida and Martin Lüscher [25].

C Sample input file

```
[Run name]
name        pedro01

[Directories]
log_dir     ./log       # absolute path, or relative path
dat_dir     ./dat       # to the working directory of iso1
cnfg_dir    ./cnfg

[MD trajectories]
nth          100        # multiple of dtr_cnfg
ntr          800        # multiple of dtr_cnfg
dtr_log      5
dtr_ms       10         # multiple of dtr_log
dtr_cnfg     50         # multiple of dtr_ms

[Random number generator]
level        0          # this should not be changed
seed         19521      # this can be any positive integer

[Boundary conditions]
type         periodic   # or SF, open, open-SF
cstar        3          # or 0, 1, 2

[SU(3) action]
beta         5.3
c0           1.0       # 1=Wilson, 5/3=Lüscher-Weisz, 3.648=Iwasaki

[U(1) action]
type         compact    # only option currently available
alpha        0.05       # bare fine-structure constant
invqel       6.0        # see "Dirac operators parameters"
c0           1.0        # Wilson action

[Quark action]
nfl          2

[Flavour 0]             # Down quark
qhat         -2         # qhat must be integer
                        # el. charge = qhat/invqel = -2/6 = -1/3
kappa        0.136377   # hopping parameter
su3csw       1.909520   # u1csw=su3csw=0 => no O(a) improv.
u1csw        1.0        # u1csw=su3csw=1 => tree-level O(a) improv.

[Flavour 1]             # Up quark
qhat         4          # el. charge = qhat/invqel = 4/6 = 2/3
kappa        0.137312
su3csw       1.909520
u1csw        1.0

[Rational 0]
power              -1 4
degree             10
range              1.98000000e-03 7.62000000e+00
mu                 0.00000000e+00
delta              5.9691841082503071e-05
A                  2.0497821359066373259 1e-01
nu[0]              1.2264797855989293316e+01
mu[0]              8.4073726152481462747 8e+00
nu[1]              3.5847504148001823054 4e+00
mu[1]              2.7973408605904763746 3e+00
nu[2]              1.3735461431317819158 7e+00
mu[2]              1.0890408975743284258 9e+00
nu[3]              5.4553438071947224496 9e-01
mu[3]              4.3359747999585790401 2e-01
nu[4]              2.1788224309816567325 6e-01
```

```
mu[4]               1.7324124034914964442 9e-01
nu[5]               8.7090117627838012359 7e-02
mu[5]               6.9246579186365189717 6e-02
nu[6]               3.4796327691166771545 2e-02
mu[6]               2.7656552058372342595 1e-02
nu[7]               1.3854025164349029891 6e-02
mu[7]               1.0984414375478649544 8e-02
nu[8]               5.3935507869481572398 9e-03
mu[8]               4.2088285805640945902 4e-03
nu[9]               1.7945677788368946670 2e-03
mu[9]               1.2301548037851647420 7e-03
x[0]                3.9203999999999997679 6e-06
x[1]                4.8183213452292917371 4e-06
x[2]                8.3193746435588951523 2e-06
x[3]                1.7576590832518868007 1e-05
x[4]                4.0928474886816771987 8e-05
x[5]                9.9416123273699013229 4e-05
x[6]                2.4572587838201178939 8e-04
x[7]                6.1168888272680862951 8e-04
x[8]                1.5269611034379659483 8e-03
x[9]                3.8161917502232446664 0e-03
x[10]               9.5411916782353490412 7e-03
x[11]               2.3858201515777680001 8e-02
x[12]               5.9649956988320484985 2e-02
x[13]               1.4907758504658469300 7e-01
x[14]               3.7214289843758080467 1e-01
x[15]               9.2638054753887877357 2e-01
x[16]               2.2897259143097370426 3e+00
x[17]               5.5617922336344652506 e+00
x[18]               1.2951070883397161281 9e+01
x[19]               2.7362113561822756224 7e+01
x[20]               4.7243771730897876182 1e+01
x[21]               5.8064399999999999124 6e+01

[HMC parameters]
actions     0 1 2 3   # List of action IDs, see below
npf         2         # Number of pseudofermions to be allocated
nlv         2         # Number of levels of integrator for MD eqs
tau         2.0       # MD trajectory length
facc        1         # Fourier acceleration for U(1) MD
                      # (0=not active, 1=active)

[Level 0]             # Innermost level
integrator  OMF4      # Omelyan-Mryglod-Folk 4th order
nstep       2         # Number of times the elementary integrator
                      # is applied at this level
forces      0 1       # List of force IDs to be integrated at
                      # this level, see below

[Level 1]             # Outermost level
integrator  OMF4
nstep       1
forces      2 3

[Action 0]            # No adjustable parameters here!
action      ACG_SU3

[Force 0]
force       FRG_SU3

[Action 1]
action      ACG_U1

[Force 1]
force       FRG_U1

[Action 2]
action   ACF_RAT_SDET # Rational approximation effective action
ipf      0            # Pseudofermion ID (a number from 0 to 1)
ifl      0            # Flavour ID (down quark)
irat     0 0 9        # Use the rational approximation with ID=0
                      # Include all rat. appr. factors, 0 -> 9,
                      # i.e. no frequency splitting
isp      0            # Solver ID, used to generate the p.f. at
                      # the beginning of the MD and to calculate
                      # the Hamiltonian at the end of the MD

[Force 2]
force    FRF_RAT_SDET
isp      1            # Solver ID, used to calculate the force

[Action 3]
action   ACF_RAT_SDET
ipf      1            # Different pseudofermion ID
ifl      1            # Different flavour ID (up quark)
irat     0 0 9
isp      0

[Force 3]
force    FRF_RAT_SDET
isp      1

[Solver 0]
solver      MSCG      # or CGNE, SAP_GCR, DFL_SAP_GCR
nmx         2048      # Maximum number of iterations
res         1.0e-11   # Residue

[Solver 1]
solver      MSCG
nmx         2048
res         1.0e-8

[Wilson flow]
integrator  RK3       # EULER: Euler, RK2: 2nd order Runge-Kutta
                      # RK3: 3rd order Runge-Kutta
eps         2.0e-2    # Integration step size
nstep       700       # Total number of integration steps
dnms        5         # Number of steps between measurements
```

References

1. (RC*), I. Campos, P. Fritzsch, M. Hansen, M. Krstić Marinković, A. Patella, A. Ramos et al., "openQ*D." GitLab: https://gitlab.com/rcstar/openQxD. CSIC: https://dx.doi.org/10.20350/digitalCSIC/8591. https://hdl.handle.net/10261/173334 (2019)
2. Simulation program for lattice QCD (openQCD code) (2016). https://cern.ch/luscher/openQCD
3. Numerical Stochastic Perturbation Theory (NSPT code) (2017). https://cern.ch/luscher/NSPT
4. (Flavour Lattice Averaging Group), S. Aoki et al., FLAG Review (2019). arXiv:1902.08191
5. V. Cirigliano, G. Ecker, H. Neufeld, A. Pich, J. Portoles, Kaon decays in the standard model. Rev. Mod. Phys. **84**, 399 (2012). arXiv:1107.6001
6. D. Giusti, V. Lubicz, G. Martinelli, C.T. Sachrajda, F. Sanfilippo, S. Simula et al., First lattice calculation of the QED corrections to leptonic decay rates. Phys. Rev. Lett. **120**, 072001 (2018). arXiv:1711.06537
7. M. Di Carlo, D. Giusti, V. Lubicz, G. Martinelli, C.T. Sachrajda, F. Sanfilippo et al., Light-meson leptonic decay rates in lattice QCD+QED. arXiv:1904.08731
8. (HFLAV), Heavy Flavor Averaging Group. https://hflav.web.cern.ch
9. S. de Boer, T. Kitahara, I. Nisandzic, Soft-photon corrections to $\bar{B} \to D\tau^-\bar{\nu}_\tau$ Relative to $\bar{B} \to D\mu^-\bar{\nu}_\mu$. Phys. Rev. Lett. **120**, 261804 (2018). arXiv:1803.05881
10. S. Calí, S. Klaver, M. Rotondo, B. Sciascia, Impacts of radiative corrections on measurements of lepton flavour universality in $B \to D\ell\nu_\ell$ decays. arXiv:1905.02702
11. S. Borsanyi et al., Ab initio calculation of the neutron–proton mass difference. Science **347**, 1452–1455 (2015). arXiv:1406.4088
12. R. Horsley et al., Isospin splittings of meson and baryon masses from three-flavor lattice QCD + QED. J. Phys. G **43**, 10LT02 (2016). arXiv:1508.06401
13. R. Horsley et al., QED effects in the pseudoscalar meson sector. JHEP **04**, 093 (2016). arXiv:1509.00799
14. A. Patella, QED corrections to hadronic observables. PoS **LATTICE2016**, 020 (2017). arXiv:1702.03857
15. D. Bernecker, H.B. Meyer, Vector correlators in lattice QCD: methods and applications. Eur. Phys. J. A **47**, 148 (2011). arXiv:1107.4388
16. T. Blum, N. Christ, M. Hayakawa, T. Izubuchi, L. Jin, C. Jung et al., Using infinite volume, continuum QED and lattice QCD for the hadronic light-by-light contribution to the muon anomalous magnetic moment. Phys. Rev. D **96**, 034515 (2017). arXiv:1705.01067
17. X. Feng, L. Jin, QED self energies from lattice QCD without power-law finite-volume errors. arXiv:1812.09817
18. B. Lucini, A. Patella, A. Ramos, N. Tantalo, Charged hadrons in local finite-volume QED+QCD with C* boundary conditions. JHEP **02**, 076 (2016). arXiv:1509.01636
19. P.A.M. Dirac, Gauge invariant formulation of quantum electrodynamics. Can. J. Phys. **33**, 650 (1955)

20. (RC*), M. Hansen, B. Lucini, A. Patella, N. Tantalo, Gauge invariant determination of charged hadron masses. JHEP **05**, 146 (2018). arXiv:1802.05474
21. G.M. de Divitiis, R. Frezzotti, V. Lubicz, G. Martinelli, R. Petronzio, G.C. Rossi et al., Leading isospin breaking effects on the lattice. Phys. Rev. D **87**, 114505 (2013). arXiv:1303.4896
22. M. Lüscher, Deflation acceleration of lattice QCD simulations. JHEP **12**, 011 (2007). arXiv:0710.5417
23. G.G. Batrouni, G.R. Katz, A.S. Kronfeld, G.P. Lepage, B. Svetitsky, K.G. Wilson, Langevin simulations of lattice field theories. Phys. Rev. D **32**, 2736 (1985)
24. S. Duane, B.J. Pendleton, Gauge invariant fourier acceleration. Phys. Lett. B **206**, 101–106 (1988)
25. M. Dalla Brida, M. Lüscher, SMD-based numerical stochastic perturbation theory. Eur. Phys. J. C **77**, 308 (2017). arXiv:1703.04396
26. M. Lüscher, S. Schaefer, Lattice QCD with open boundary conditions and twisted-mass reweighting. Comput. Phys. Commun. **184**, 519–528 (2013). arXiv:1206.2809
27. M. Lüscher, R. Narayanan, P. Weisz, U. Wolff, The Schrödinger functional: a renormalizable probe for nonAbelian gauge theories. Nucl. Phys. B **384**, 168–228 (1992). arXiv:9207009
28. S. Sint, On the Schrödinger functional in QCD. Nucl. Phys. B **421**, 135–158 (1994). arXiv:9312079
29. M. Lüscher, Step scaling and the Yang–Mills gradient flow. JHEP **06**, 105 (2014). arXiv:1404.5930
30. A.S. Kronfeld, U.J. Wiese, SU(N) gauge theories with C periodic boundary conditions. 1. Topological structure. Nucl. Phys. B **357**, 521–533 (1991)
31. A.S. Kronfeld, U.J. Wiese, SU(N) gauge theories with C periodic boundary conditions. 2. Small volume dynamics. Nucl. Phys. B **401**, 190–205 (1993). arXiv:9210008
32. U.J. Wiese, C periodic and G periodic QCD at finite temperature. Nucl. Phys. B **375**, 45–66 (1992)
33. L. Polley, Boundaries for $SU(3)_C \times U(1)_{el}$ lattice gauge theory with a chemical potential. Z. Phys. C **59**, 105–108 (1993)
34. I. Montvay, Supersymmetric Yang–Mills theory on the lattice. Int. J. Mod. Phys. A **17**, 2377–2412 (2002). arXiv:0112007
35. S. Ali, G. Bergner, H. Gerber, P. Giudice, I. Montvay, G. Münster et al., The light bound states of $\mathcal{N} = 1$ supersymmetric SU(3) Yang–Mills theory on the lattice. JHEP **03**, 113 (2018). arXiv:1801.08062
36. T.A. DeGrand, A conditioning technique for matrix inversion for Wilson Fermions. Comput. Phys. Commun. **52**, 161–164 (1988)
37. A.D. Kennedy, I. Horvath, S. Sint, A New exact method for dynamical fermion computations with nonlocal actions. Nucl. Phys. Proc. Suppl. **73**, 834–836 (1999). arXiv:9809092 ([,834(1998)])
38. M. Lüscher, F. Palombi, Fluctuations and reweighting of the quark determinant on large lattices. PoS **LATTICE2008**, 049 (2008). arXiv:0810.0946
39. J.C. Sexton, D.H. Weingarten, Hamiltonian evolution for the hybrid Monte Carlo algorithm. Nucl. Phys. B **380**, 665–677 (1992)
40. I. Omelyan, I. Mryglod, R. Folk, Symplectic analytically integrable decomposition algorithms: classification, derivation, and application to molecular dynamics, quantum and celestial mechanics simulations. Comput. Phys. Commun. **151**, 272–314 (2003)
41. I. Campos, P. Fritzsch, M. Hansen, M.K. Marinković, A. Patella, A. Ramos et al., openQ*D simulation code for QCD + QED. EPJ Web Conf. **175**, 09005 (2018). arXiv:1710.08839
42. (RC*), "openQ*D documentation, Gauge actions,`doc/gauge_action.pdf`."
43. (RC*), "openQ*D documentation, Dirac operator, `doc/dirac.pdf`."
44. M. Lüscher, S. Sint, R. Sommer, P. Weisz, Chiral symmetry and O(a) improvement in lattice QCD. Nucl. Phys. B **478**, 365–400 (1996). arXiv:9605038
45. M. Lüscher, A portable high quality random number generator for lattice field theory simulations. Comput. Phys. Commun. **79**, 100–110 (1994). arXiv:9309020
46. E. Remes, Sur le calcul effectif des polynômes d'approximation de Tchebichef. C. R. Acad. Sci. Paris **199**, 337–340 (1934)
47. A. Ralston, Rational Chebyshev approximation by Remes' algorithms. Numerische Mathematik **7**, 322–330 (1965)
48. M. Hansen, B. Lucini, A. Patella, N. Tantalo, Simulations of QCD and QED with C* boundary conditions. EPJ Web Conf. **175**, 09001 (2018). arXiv:1710.08838
49. J. Bulava, S. Schaefer, Improvement of $N_f = 3$ lattice QCD with Wilson fermions and tree-level improved gauge action. Nucl. Phys. B **874**, 188–197 (2013). arXiv:1304.7093
50. (ALPHA), K. Jansen, R. Sommer, O(a) improvement of lattice QCD with two flavors of Wilson quarks. Nucl. Phys. B **530**, 185–203 (1998). arXiv:9803017. (**Erratum: Nucl. Phys.B643,517(2002)**)
51. P. Fritzsch, F. Knechtli, B. Leder, M. Marinkovic, S. Schaefer, R. Sommer et al., The strange quark mass and Lambda parameter of two flavor QCD. Nucl. Phys. B **865**, 397–429 (2012). arXiv:1205.5380
52. M. Bruno, T. Korzec, S. Schaefer, Setting the scale for the CLS $2 + 1$ flavor ensembles. Phys. Rev. D **95**, 074504 (2017). arXiv:1608.08900
53. M. Lüscher, Local coherence and deflation of the low quark modes in lattice QCD. JHEP **07**, 081 (2007). arXiv:0706.2298
54. A. Frommer, K. Kahl, S. Krieg, B. Leder, M. Rottmann, Adaptive aggregation based domain decomposition multigrid for the lattice Wilson Dirac operator. SIAM J. Sci. Comput. **36**, A1581–A1608 (2014). arXiv:1303.1377
55. M. Bruno et al., Simulation of QCD with $N_f = 2 + 1$ flavors of non-perturbatively improved Wilson fermions. JHEP **02**, 043 (2015). arXiv:1411.3982
56. M. Lüscher, Properties and uses of the Wilson flow in lattice QCD. JHEP **08**, 071 (2010). arXiv:1006.4518 (Erratum: JHEP03,092(2014))
57. M. Lüscher, Chiral symmetry and the Yang-Mills gradient flow. JHEP **04**, 123 (2013). arXiv:1302.5246
58. A. Francis, P. Fritzsch, M. Lüscher, A. Rago, Master-field simulations of O(a)-improved lattice QCD: algorithms, stability and exactness. arXiv:1911.04533
59. M. Hasenbusch, Speeding up the hybrid Monte Carlo algorithm for dynamical fermions. Phys. Lett. B **519**, 177–182 (2001). arXiv:0107019